



## Exploring the bottlenecks of anionic redox in Li-rich layered sulfides

Sujoy Saha, Gaurav Assat, Moulay Tahar Sougrati, Dominique Foix, Haifeng Li, Jean Vergnet, Soma Turi, Yang Ha, Wanli Yang, Jordi Cabana, et al.

### ► To cite this version:

Sujoy Saha, Gaurav Assat, Moulay Tahar Sougrati, Dominique Foix, Haifeng Li, et al.. Exploring the bottlenecks of anionic redox in Li-rich layered sulfides. *Nature Energy*, 2019, 4 (11), pp.977-987. 10.1038/s41560-019-0493-0 . hal-02378228

**HAL Id: hal-02378228**

**<https://hal.science/hal-02378228>**

Submitted on 3 Nov 2020

**HAL** is a multi-disciplinary open access archive for the deposit and dissemination of scientific research documents, whether they are published or not. The documents may come from teaching and research institutions in France or abroad, or from public or private research centers.

L'archive ouverte pluridisciplinaire **HAL**, est destinée au dépôt et à la diffusion de documents scientifiques de niveau recherche, publiés ou non, émanant des établissements d'enseignement et de recherche français ou étrangers, des laboratoires publics ou privés.

# Lawrence Berkeley National Laboratory

## Recent Work

**Title**

Exploring the bottlenecks of anionic redox in Li-rich layered sulfides

**Permalink**

<https://escholarship.org/uc/item/2n5061wm>

**Journal**

Nature Energy, 4(11)

**ISSN**

2058-7546

**Authors**

Saha, S  
Assat, G  
Sougrati, MT  
et al.

**Publication Date**

2019-11-01

**DOI**

10.1038/s41560-019-0493-0

Peer reviewed

# Exploring the Bottlenecks of Anionic Redox in Li-rich Layered Sulfides

Sujoy Saha<sup>1,2,3†</sup>, Gaurav Assat<sup>1,2,3†</sup>, Moulay Tahar Sougrati<sup>3,4,5</sup>, Dominique Foix<sup>3,6</sup>, Haifeng Li<sup>7</sup>, Jean Vergnet<sup>1,3</sup>, Soma Turi<sup>1</sup>, Yang Ha<sup>8</sup>, Wanli Yang<sup>8</sup>, Jordi Cabana<sup>7</sup>, Gwenaëlle Rousse<sup>1,2,3</sup>, Artem M. Abakumov<sup>9</sup>, Jean-Marie Tarascon<sup>1,2,3\*</sup>

<sup>1</sup>Collège de France, Chaire de Chimie du Solide et de l'Energie, UMR 8260, 11 Place Marcelin Berthelot, 75231 CEDEX 05 Paris, France

<sup>2</sup>Sorbonne Université, 4 Place Jussieu, F-75005 Paris, France

<sup>3</sup>Réseau sur le Stockage Electrochimique de l'Energie (RS2E), FR CNRS 3459, 33 Rue Saint Leu, 80039 Amiens, France

<sup>4</sup>Institut Charles Gerhardt - UMR 5253, 34095 Montpellier Cedex 5, France

<sup>5</sup>ALISTORE-European Research Institute, 33 rue Saint-Leu, 80039 Amiens Cedex, France

<sup>6</sup>IPREM/ECP (UMR 5254), Université de Pau, 2 Avenue Pierre Angot, 64053 Pau Cedex 9, France

<sup>7</sup>Department of Chemistry, University of Illinois at Chicago, Chicago, Illinois 60607, United States

<sup>8</sup>Advanced Light Source, Lawrence Berkeley National Laboratory, One Cyclotron Road, Berkeley, CA 94720, USA

<sup>9</sup>Center for Energy Science and Technology, Skolkovo Institute of Science and Technology, Nobel Str. 3, 143026 Moscow, Russia

<sup>†</sup> These authors contributed equally to this work.

\*e-mail: [jean-marie.tarascon@college-de-france.fr](mailto:jean-marie.tarascon@college-de-france.fr)

## Abstract

To satisfy the long-awaited need of new lithium-ion battery cathode materials with higher energy density, anionic redox chemistry has emerged as a new paradigm that is responsible for the high capacity in Li-rich layered oxides, for example, in  $\text{Li}_{1.2}\text{Ni}_{0.13}\text{Mn}_{0.54}\text{Co}_{0.13}\text{O}_2$  (Li-rich NMC). However, their market-implementation has been plagued by certain bottlenecks originating intriguingly from the anionic redox activity itself. To fundamentally understand these bottlenecks (voltage fade, hysteresis and sluggish kinetics), we decided to target the ligand by switching to isostructural Li-rich layered sulfides. Herein, we designed new  $\text{Li}_{1.33-2y/3}\text{Ti}_{0.67-y/3}\text{Fe}_y\text{S}_2$  cathodes that enlist sustained reversible capacities of  $\sim 245 \text{ mAh}\cdot\text{g}^{-1}$  due to cumulated cationic ( $\text{Fe}^{2+/3+}$ ) and anionic ( $\text{S}^{2-} / \text{S}^{n-}$ ,  $n < 2$ ) redox processes. In-depth electrochemical analysis revealed nearly zero irreversible capacity during the initial cycle, very small voltage fade upon long cycling, with low voltage hysteresis and fast kinetics, which contrasts positively with respect to their Li-rich NMC oxide analogues. Our study, further complemented with DFT calculations, demonstrates that moving from oxygen to sulfur as the ligand is an adequate strategy to partially mitigate the practical bottlenecks affecting anionic redox, although with an expected penalty in cell voltage. Altogether the present findings provide chemical clues on improving the holistic performance of anionic redox electrodes via ligand tuning, and hence strengthen the feasibility to ultimately capitalize on the energy benefits of oxygen redox.

## Introduction

Over the past three decades, Li-ion batteries (LIB) have revolutionized the portable electronics industry, while more recently reorienting the automotive industry by enabling electric vehicles.<sup>1,2</sup> To comply with the ever-growing demands of energy for such applications, increasing the energy density of LIBs has become a formidable challenge. For many years, the cathode materials in LIBs relied solely on the transition metal (cationic) redox, until the recently discovered anionic redox, i.e., electrochemical participation of the oxygen ligands, became a new approach for designing higher energy cathode materials. Li-rich Mn-based layered oxides, for example,  $\text{Li}_{1.2}\text{Ni}_{0.2}\text{Mn}_{0.6}\text{O}_2$  and  $\text{Li}_{1.2}\text{Ni}_{0.13}\text{Mn}_{0.54}\text{Co}_{0.13}\text{O}_2$  (Li-rich NMC) hold the highest promises in this regard, as these cathodes can deliver a specific energy approaching  $\sim 1000 \text{ Wh}\cdot\text{kg}^{-1}$  at the material-level. These materials can potentially replace the currently used NMCs (e.g.  $\text{LiNi}_{0.6}\text{Mn}_{0.2}\text{Co}_{0.2}\text{O}_2$ ,  $\sim 700 \text{ Wh}\cdot\text{kg}^{-1}$ ). Thanks to a decade of intense research, it is now well established that the anomalous extra capacity of Li-rich cathodes arises from the redox of  $\text{O}^{2-}$  anions, more specifically the ‘non-bonding’ O  $2p$  orbitals that point towards excess-Li in the metal layers.<sup>3–8</sup> Invigorated by this fundamental understanding, solid-state chemists have extended the concept of oxygen redox to cation-disordered  $\text{Li}_{1+y}\text{M}_{1-y}\text{O}_2$  ( $\text{M} = \text{Nb}, \text{Mn}, \text{Ti}, \text{Fe}, \text{V} \dots$ ) as well as Na-based layered oxides.<sup>9–11</sup> Despite this rich materials design-space, certain practical issues, such as voltage fade, poor kinetics, voltage hysteresis, and irreversible  $\text{O}_2$  loss, have delayed the commercialization of Li-rich NMCs.<sup>12</sup> Although the crucial role of oxygen redox towards these issues was clearly highlighted by detailed investigations on a ‘practical’ Li-rich NMC and also on a ‘model’  $\text{Li}_{1.33}\text{Ru}_{0.5}\text{Sn}_{0.17}\text{O}_2$  electrode, much remains to be understood for further fundamental insights that will ultimately lead to implementable solutions.<sup>12–14</sup> Therefore, time has come to reinject the Li-rich systems with a fresh perspective towards the above-mentioned practical roadblocks observed in oxides. So far, only two materials-composition parameters were explored in Li-rich layered oxides, i.e. (i) going down from  $3d$  Mn to  $4d$  Ru and  $5d$  Ir for stabilizing oxygen redox and (ii) increasing the Li-rich character to access higher capacity (e.g.  $\text{Li}_3\text{IrO}_4$ ).<sup>15–17</sup> More recently, a third approach with mild success has emerged, that is to tune the ligand by increasing electronegativity of the anionic sublattice via substituting fluorine for oxygen, but so far limited only to disordered rocksalt structures.<sup>18,19</sup> Herein, we decided to explore a fourth direction by replacing the ligand oxygen with sulfur to design new Li-rich layered sulfides. Because sulfur is larger, softer and less electronegative compared to oxygen, anionic redox in sulfides can be expected to behave differently and possibly provide clues towards better performances.

Early sulfide electrodes, although long forgotten after the emergence of layered oxide cathodes, played a crucial historical role. To recall, the path towards modern Li-ion technology was paved by attempts of commercialization of Li-free layered transition-metal chalcogenides, such as  $\text{TiS}_2$ ,  $\text{MoS}_2$  etc., way back in the 1970s, which was rapidly terminated because of safety issues due to Li-metal dendrite formation.<sup>20,21</sup> Interestingly, unlike oxides, stable ligand-hole chemistry was well-known in sulfides, e.g.,  $\text{TiS}_3$  (believed to exist as  $\text{Ti}^{4+}\text{S}^{2-}(\text{S}_2)^{2-}$ ),  $\text{Fe}^{2+}(\text{S}_2)^{2-}$ , etc., since the pioneering works by Rouxel *et al.*<sup>22,23</sup> In such materials, S exists fully or partially as dimerized  $\text{S}^--\text{S}^-$  pairs and undergoes breaking of S—S bonds to regain the standard  $\text{S}^{2-}$  state upon electrochemical insertion of Li.<sup>24–29</sup> However, Li (de)intercalation is only partly reversible in such materials besides rapid capacity fading.<sup>30–32</sup> Further studying the poly-sulfides such as  $\text{TiS}_4$  and  $\text{VS}_4$ , mainly for their conversion-type mechanism leading to large capacities at low potential, researchers have noted that such compounds were also enlisting sulfur redox activity.<sup>33–37</sup> Similarly, by reinvestigating the crystalline  $\text{LiMS}_2$  ( $\text{M} = \text{Ti}, \text{V}, \text{Cr}, \text{Fe}$ ) layered sulfides directly prepared from solid-state reactions, scientists also found that in some of these phases, both Li removal and insertion are possible, but it remains unclear whether the process involves anionic besides cationic redox activity.<sup>38–40</sup> Thus,

deciphering the sulfur redox process in such compounds could be of paramount importance to further understand the oxygen redox in Li-rich layered oxides.

Li-rich NMCs are derived from the layered  $\text{Li}_{1.33}\text{Mn}_{0.67}\text{O}_2$  (commonly written as  $\text{Li}_2\text{MnO}_3$ ) with their anionic redox activity being a function of the competition between  $U$  ( $d$ - $d$  coulomb interaction) and  $\Delta$  (charge transfer) terms.<sup>41</sup> Preparing a similar Li-rich Mn-based layered sulfide is not possible, simply because the S  $3p$  band is situated much closer to the Li/Li<sup>+</sup> reference than the O  $2p$  band, leaving the Mn<sup>3+/4+</sup> redox band too low-lying, see Figure 1a,b. Hence to design an analogous layered sulfide  $\text{Li}_{1.33}\text{M}_{0.67}\text{S}_2$ , an appropriate transition metal M needs to be chosen first. Amongst  $3d$  metals, M = Ti<sup>4+</sup> presents the best choice for sulfides, because the Ti<sup>3+/4+</sup> redox band is located above the S  $3p$  band. However, since Ti<sup>4+</sup> has  $3d^0$  electronic configuration,  $\text{Li}_{1.33}\text{Ti}_{0.66}\text{S}_2$  is apparently electrochemically inactive, as shown recently, even though it has a high theoretical capacity of 339 mAh·g<sup>-1</sup> (considering removal of all Li's).<sup>42</sup> This situation reminds that of the  $\text{Li}_{1.33}\text{Mn}_{0.67}\text{O}_2$  phase (poor electrochemical performance without nano-sizing) that required partial substitution with Ni<sup>2+</sup> to instigate electrochemical activity (Figure 1a).<sup>43-45</sup> A first hint to address this problem in sulfides consists, as discussed by Li *et al.*, in using Co<sup>2+</sup> as a substituent (owing to its large  $U$  and small  $\Delta$ ) to initiate reversible anionic redox.<sup>42</sup> Pursuing their idea, the authors succeeded in preparing  $\text{Li}_{1.2}\text{Ti}_{0.6}\text{Co}_{0.2}\text{S}_2$  showing anionic redox activity.<sup>42</sup> Other successful strategies to adjust proper band positioning have consisted in either preparing Ti<sup>3+</sup>-doped  $\text{Li}_{1.33-y/3}\text{Ti}_{0.67-2y/3}^{4+}\text{Ti}_{y/3}^{3+}\text{S}_2$ , or triggering antisite occupation as shown for  $\text{NaCr}^{3+}\text{S}_2$ , or preparing  $\text{Li}_{1.33}\text{Ti}_{0.67}^{4+}\text{S}_2$  and  $\text{Li}_{1.5}\text{Nb}^{5+}_{0.5}\text{S}_2$  having disordered rock-salt structures.<sup>46-49</sup> We herein demonstrate the feasibility to activate the anionic redox activity in Li-rich layered  $\text{Li}_{1.33-2y/3}\text{Ti}_{0.67-y/3}^{4+}\text{Fe}_{y/3}^{2+}\text{S}_2$  via the use of Fe substitution. This situation is favourable for reversible sulfur redox, since the Fe<sup>2+/3+</sup> redox couple with available electrons ( $3d^6$ ) is expected to be pinned at the top of the S  $3p$  band (Figure 1c).<sup>38</sup> We isolate the  $\text{Li}_{1.13}\text{Ti}_{0.57}\text{Fe}_{0.3}\text{S}_2$  compound showing, based on cumulated cationic and anionic redox activity, a sustained reversible capacity of ~245 mAh·g<sup>-1</sup> at an average voltage of ~2.5 V, hence leading to a specific energy of ~600 Wh·kg<sup>-1</sup> that compares favorably with  $\text{LiCoO}_2$ . Moreover, we demonstrate the advantages of choosing a softer ligand in partially mitigating both voltage fade and hysteresis without any compromise in kinetics, hence providing confidence about the feasibility of better capitalizing on the benefits of the anionic redox.

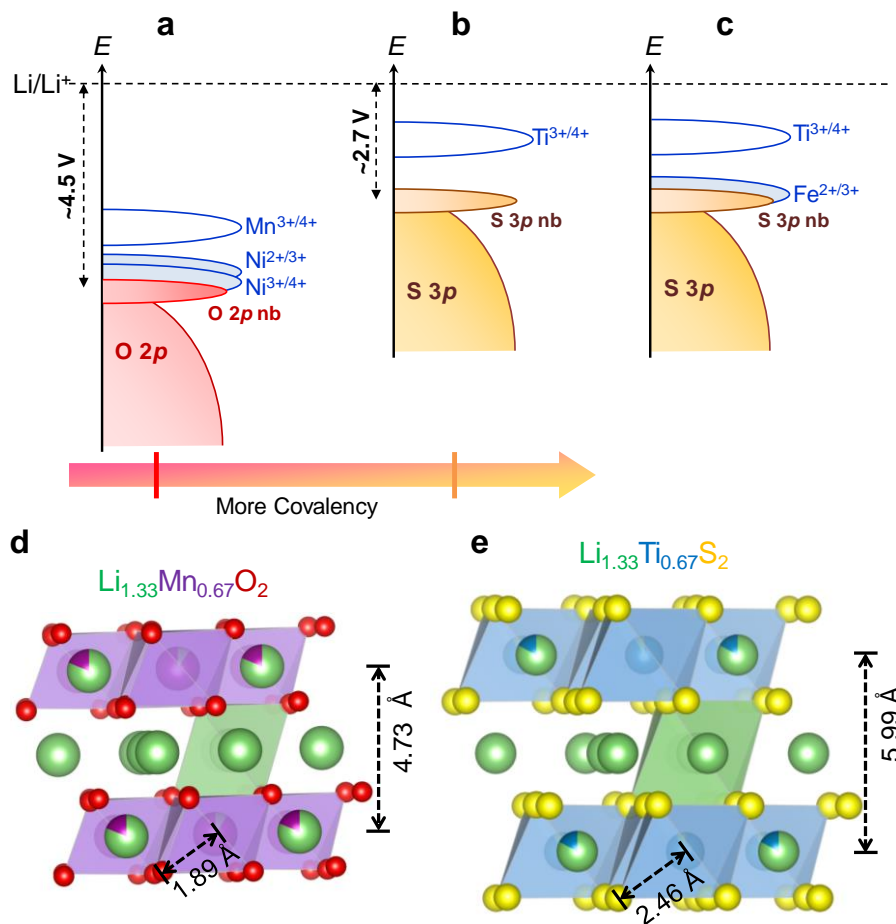


**Figure 1. Moving from Li-rich layered oxides to sulfides.** Schematic band structure of  $\text{Ni}^{2+}$  substituted  $\text{Li}_{1.33}\text{Mn}_{0.67}\text{O}_2$  (a) and  $\text{Li}_{1.33}\text{Ti}_{0.67}\text{S}_2$  (b) and its  $\text{Fe}^{2+}$  substituted derivative (c). The relative band positions are estimated based on *Ref*<sup>3,38</sup>. The label *nb* stands for non-bonding. The crystal structures of  $\text{Li}_{1.33}\text{Mn}_{0.67}\text{O}_2$  (d, adapted from the *Ref*<sup>50</sup>) and  $\text{Li}_{1.33}\text{Ti}_{0.67}\text{S}_2$  (e, this work), indicating the layer gap and the average metal-ligand bond distance.

## Results

Nominal compositions of  $\text{Li}_{1.33-2y/3}\text{Ti}_{0.67-y/3}\text{Fe}_y\text{S}_2$ , with  $y = 0 - 0.5$ , were prepared by reacting  $\text{Li}_2\text{S}$ ,  $\text{TiS}_2$  and  $\text{FeS}$  in stoichiometric amounts in vacuum-sealed quartz tubes at  $750^\circ\text{C}$  (see the Experimental Section for details). The X-ray diffraction (XRD) patterns are gathered in Figure S1a for all the compositions. The XRD pattern of the unsubstituted  $\text{Li}_{1.33}\text{Ti}_{0.67}\text{S}_2$  (without Fe,  $y = 0$ ) phase could be refined in the  $C2/m$  space group alike for  $\text{Li}_{1.33}\text{Mn}_{0.67}\text{O}_2$ . The Rietveld refinement of its synchrotron XRD (SXRD) pattern is shown in Figure S1b with the obtained parameters summarized in Table S1. This crystal structure is similar to honeycomb-ordered Li-rich layered oxides, however with an expectedly larger unit cell to accommodate the bulkier S atoms, see Figure 1d,e. Upon increasing the Fe content  $y$ , there is a progressive shift of the Bragg peaks (Figure 2a) indicating the existence of a solid solution. Moreover, Fe-containing compositions ( $y = 0.1 - 0.5$ ) do not show the superstructure peaks (Figure S1a), most likely because  $\text{Fe}^{2+}$  disrupts the honeycomb  $\text{Li}^+/\text{Ti}^{4+}$  ordering. Therefore, the Fe-containing phases could be fitted in a hexagonal

$R\bar{3}m$  description analogous to the well-known Li-rich layered  $\text{Li}_{1+y}\text{M}_{1-y}\text{O}_2$  phases, with the obtained lattice parameters shown in Figure 2b. With increasing Fe content, we observe a monotonic increase in the  $c$  parameter that is accompanied by a decrease in the  $a$  parameter, such that the overall effect is a monotonic decrease in unit cell volume ( $V$ ). Since among the  $\text{Li}_{1.33-2y/3}\text{Ti}_{0.67-y/3}\text{Fe}_y\text{S}_2$  series, the compound with  $y = 0.3$  will be the center of interest in this study, we also performed the Rietveld refinement of its SXRD pattern (Figure 2c), which confirms that Fe, Ti and Li occupy same site in the metal layer (see the structural model in Table S2). This structure was further confirmed by Rietveld refinement of its neutron powder diffraction (NPD) pattern (see Figure S5a).

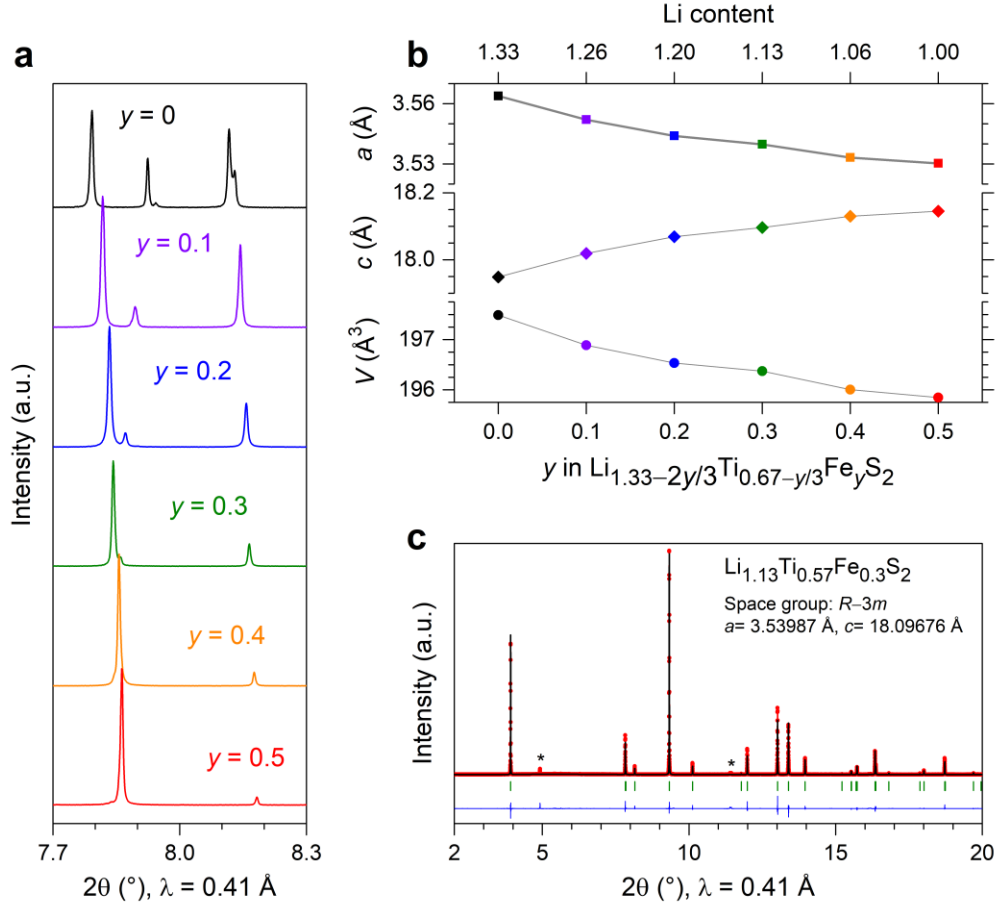


**Figure 2. Structural behavior of the  $\text{Li}_{1.33-2y/3}\text{Ti}_{0.67-y/3}\text{Fe}_y\text{S}_2$  series.** (a) SXRD patterns and (b) variation of lattice parameters (obtained from the Rietveld refinement of the SXRD patterns). In (b), for the  $y = 0$  composition, the lattice parameters have been converted to the  $R\bar{3}m$  description. (c) Rietveld refinement of the SXRD pattern of the  $\text{Li}_{1.13}\text{Ti}_{0.57}\text{Fe}_{0.3}\text{S}_2$  sample. The red circles, black continuous line, blue line, and green tick bars represent the observed, calculated and difference patterns, and Bragg positions, respectively. Note that minor  $\text{Li}_2\text{TiO}_3$  impurity (indicated with \*) was detected in the SXRD pattern, probably due to minor air-leakage during the preparation of the sample-capillary prior to the acquisition of SXRD patterns.

The electrochemical performances of the  $\text{Li}_{1.33-2y/3}\text{Ti}_{0.67-y/3}\text{Fe}_y\text{S}_2$  samples were tested in Li-half cells between 1.8 V and 3 V at a rate of C/20 and the voltage profiles are summarized in Figure 3a and S2a. The unsubstituted  $\text{Li}_{1.33}\text{Ti}_{0.67}\text{S}_2$  ( $y = 0$ ) shows very poor electrochemical activity since only 0.1 Li could be extracted reversibly. Attempts to enhance the activity by either ball milling the samples or by adding larger amounts of carbon additive were unsuccessful, hence leading us to conclude that such a non-activity is intrinsic to the phase and most likely nested in the fact that the  $\text{Ti}^{3+/4+}$  redox band is empty and is situated far above the S 3p band, hence unable to stabilize oxidized sulfur (Figure 1b). This contrasts with the  $\text{Fe}^{2+}$ -containing phases (Figure 1c) that are electrochemically active, which show a specificity that is nested in the second cycle's charge trace which mismatches the first one because it occurs at a lower potential (Figure 3a). Note also the appearance of a short sloped voltage (marked by 'S' in Figure 3a) at the early stage of charge, and most likely related to Fe redox activity. This contrasts with a long plateau-like (marked by 'P') activity on further oxidation. Lastly, the corresponding  $dQ/dV$  profiles are shown in Figure 3b and S2c, which clearly highlights that the respective oxidation potentials shift to lower voltage with a systematic decrease in hysteresis (Figure S2e) upon increasing the Fe content. After the first cycle, note that the subsequent charge and discharge profiles are very similar (see Figure S2b for  $\text{Li}_{1.13}\text{Ti}_{0.57}\text{Fe}_{0.3}\text{S}_2$ ) with the polarization gradually reducing to ~100 mV for the  $y = 0.3$  composition, instead of ~220 mV during the first cycle. This indicates that the first cycle acts as an 'activation' cycle alike the Li-rich NMC oxides. The variation of capacity as a function of the Fe-content shows a bell-shape type behaviour which peaks at 245  $\text{mAh}\cdot\text{g}^{-1}$  for the composition  $\text{Li}_{1.13}\text{Ti}_{0.57}\text{Fe}_{0.3}\text{S}_2$  ( $y = 0.3$ ). Even by assuming full utilization of the multi-electron oxidation of  $\text{Fe}^{2+}$  to  $\text{Fe}^{4+}$ , which is quite unlikely to occur in sulfide frameworks, we cannot account for all the measured capacity, hence implying the activity of the anionic network, see Figure 3c. The capacity decrease beyond  $y > 0.3$  is simply due to the lower amount of available Li in the  $\text{Li}_{1.33-2y/3}\text{Ti}_{0.67-y/3}\text{Fe}_y\text{S}_2$  samples when the Fe content ( $y$ ) increases. In contrast the raise noted until  $y = 0.3$  is most likely nested in the gradual amelioration of the band positioning with introduction of Fe content that triggers reversible anionic redox activity. Among the various Fe compositions studied, the  $y = 0.3$  sample not only shows the largest capacity, but also a respectable capacity retention (Figure 3d and S2d) with also barely noticeable irreversible capacity in the first discharge. Thus, we chose this composition for further investigation, starting by exploring whether the activation process over the first cycle is related to structural aspects.



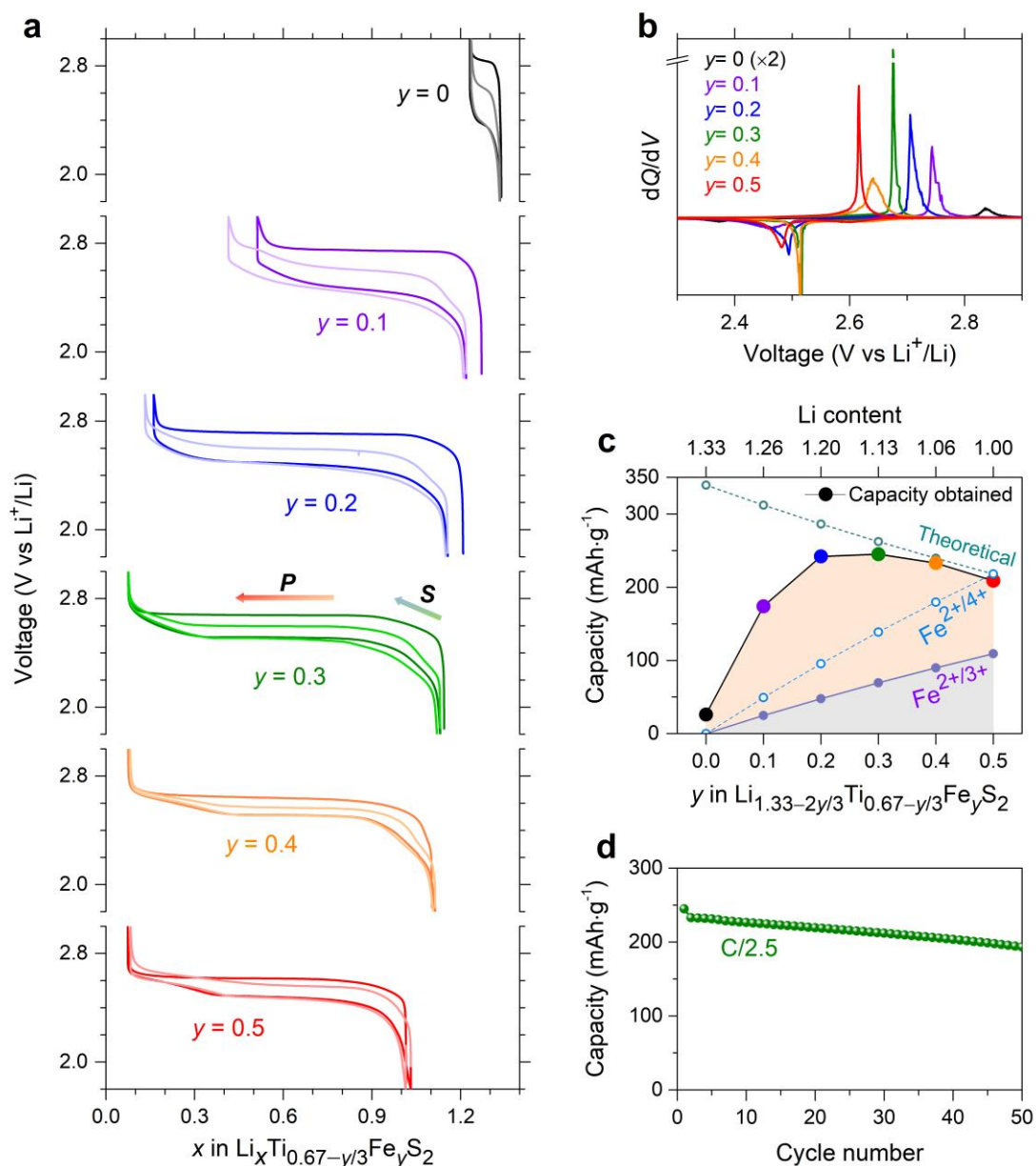


**Figure 3. Electrochemical behavior of  $\text{Li}_{1.33-2y/3}\text{Ti}_{0.67-y/3}\text{Fe}_y\text{S}_2$ .** (a) Voltage profiles of the compositions obtained over cycling vs Li at C/20 for the first two cycles. The curves in lighter colors denote the second cycles. The arrows marked by 'S' and 'P' denote the slope and the plateau, respectively. (b)  $dQ/dV$  curves obtained in the first cycle for the various compositions. (c) Theoretical capacity (considering total Li-removal) and the actual discharge capacity obtained for the compounds over cycling at C/20. The capacity expected from cationic  $\text{Fe}^{2+/3+}$  and hypothetical  $\text{Fe}^{2+/4+}$  redox is also shown. (d) Cycling performance of a  $\text{Li}_{1.13}\text{Ti}_{0.57}\text{Fe}_{0.3}\text{S}_2/\text{Li}$  half-cell at a rate of C/2.5 (except the first formation cycle at C/20). The material was cycled as powder (mixed with 20 wt% C, see Figure S2d inset) in a Swagelok type cell, without any further optimization.

To better understand the structural evolution pertaining to the  $\text{Li}_{1.13}\text{Ti}_{0.57}\text{Fe}_{0.3}\text{S}_2$  phase during the Li uptake-removal process, operando XRD measurements were conducted and XRD patterns were collected for every change in lithium stoichiometry of  $\sim 0.1$  (Fig. 4). Upon charge, we observed a slight initial shift of the main peaks, indicating solid-solution behaviour. Over this regime, the unit cell volume decreases as a consequence of an anisotropic variation of the  $a$  and  $c$  lattice parameters (see also, Figure S3a). Then, as the voltage reaches the first plateau, there is a gradual change in the intensity of the peaks with some peaks disappearing at the expense of new ones, which sharpen to give a well-defined XRD powder pattern at the end of the full charge, hence suggesting a two-phase de-intercalation process. This new phase with approximate composition  $\text{Li}_{0.13}\text{Ti}_{0.57}\text{Fe}_{0.3}\text{S}_2$ , whose structure remains as layered one as described in detail in the next paragraph, has a lower unit cell volume (by  $\sim 12.2\%$ ) than the pristine one. On discharge, the compound undergoes first a solid-solution process for which both the  $a$  and  $c$  lattice parameters strongly increase (Figure S3a). Then, a biphasic process is observed with the growth of a phase with increased volume, followed again by solid-solution behaviour. We therefore have, for the first cycle, charge and discharge processes that proceed through different structural paths, even though the pattern returns close to the one for the pristine phase (see Figure S3b). This path-difference can be clearly observed from the evolution of the unit cell volume (Figure 4a) and of the  $a$  and  $c$  lattice parameters (see Figure S3a). On the other hand, over the 2<sup>nd</sup> cycle, the XRD patterns indicate more symmetric, although not perfect, pathways on charge and discharge (Figure S4). Overall, throughout cycling the phase remains crystalline with well-preserved long-range layered crystal structure.

Next, an in-depth exploration of the crystal structures at different states of charge (pristine, fully-charged and fully-discharged after first cycle) was undertaken using SXRD. In agreement with the lab XRD data, the patterns can be indexed in the  $R\bar{3}m$  space group. The pristine  $\text{Li}_{1.13}\text{Ti}_{0.57}\text{Fe}_{0.3}\text{S}_2$  ( $V = 196.384(2) \text{ \AA}^3$ ) presents an average Ti–S bond-length of  $2.4792(3) \text{ \AA}$ , with average S–S distances of  $\sim 3.505 \text{ \AA}$  (see the structural model in Table S2). The Rietveld refinement of the SXRD pattern of the fully-charged  $\text{Li}_{0.13}\text{Ti}_{0.57}\text{Fe}_{0.3}\text{S}_2$  phase (Figure 4b) indicates a much smaller unit cell ( $V = 172.338(6) \text{ \AA}^3$ ) (see Table S3 for the structural model). Moreover the average Ti–S bond length was found to shrink to  $2.3635(1) \text{ \AA}$ , leading to decreased average S–S distances of  $\sim 3.344 \text{ \AA}$ .

In parallel, we collected the selected-area electron diffraction (SAED) of the fully-charged phase which could again be successfully indexed with an  $R\bar{3}m$  unit cell (Figure S5b). The corresponding high angle annular dark field scanning transmission electron microscopy (HAADF-STEM) image shows only the (Ti/Fe) $\text{S}_2$  layers. The HAADF intensity profile (inset, Figure 4c) clearly demonstrates no scattering density between the (Ti/Fe) $\text{S}_2$  layers and thus discards the possibility of transition-metal migration to the interlayer sites (Figure 4c). The Rietveld refinement of SXRD pattern (Figure S5c, Table S4) of the fully-discharged sample is very similar to the pristine phase ( $V = 196.896(2) \text{ \AA}^3$ ) with an average Ti–S bond length of  $2.4825(3) \text{ \AA}$  and average S–S distance of  $3.51(2) \text{ \AA}$ . Worth mentioning is that such S–S distances are quite larger than the  $(\text{S–S})^{2-}$  bond lengths reported early on for  $\text{TiS}_3$  ( $2.04 \text{ \AA}$ ) (Figure 4d) suggesting either an absence of complete dimerization in  $\text{Li}_{0.13}\text{Ti}_{0.57}\text{Fe}_{0.3}\text{S}_2$  or a possible error in the reported  $\text{TiS}_3$  structure.<sup>51</sup> Further investigations focusing specifically on the local structure of such sulfide compounds are hence planned.

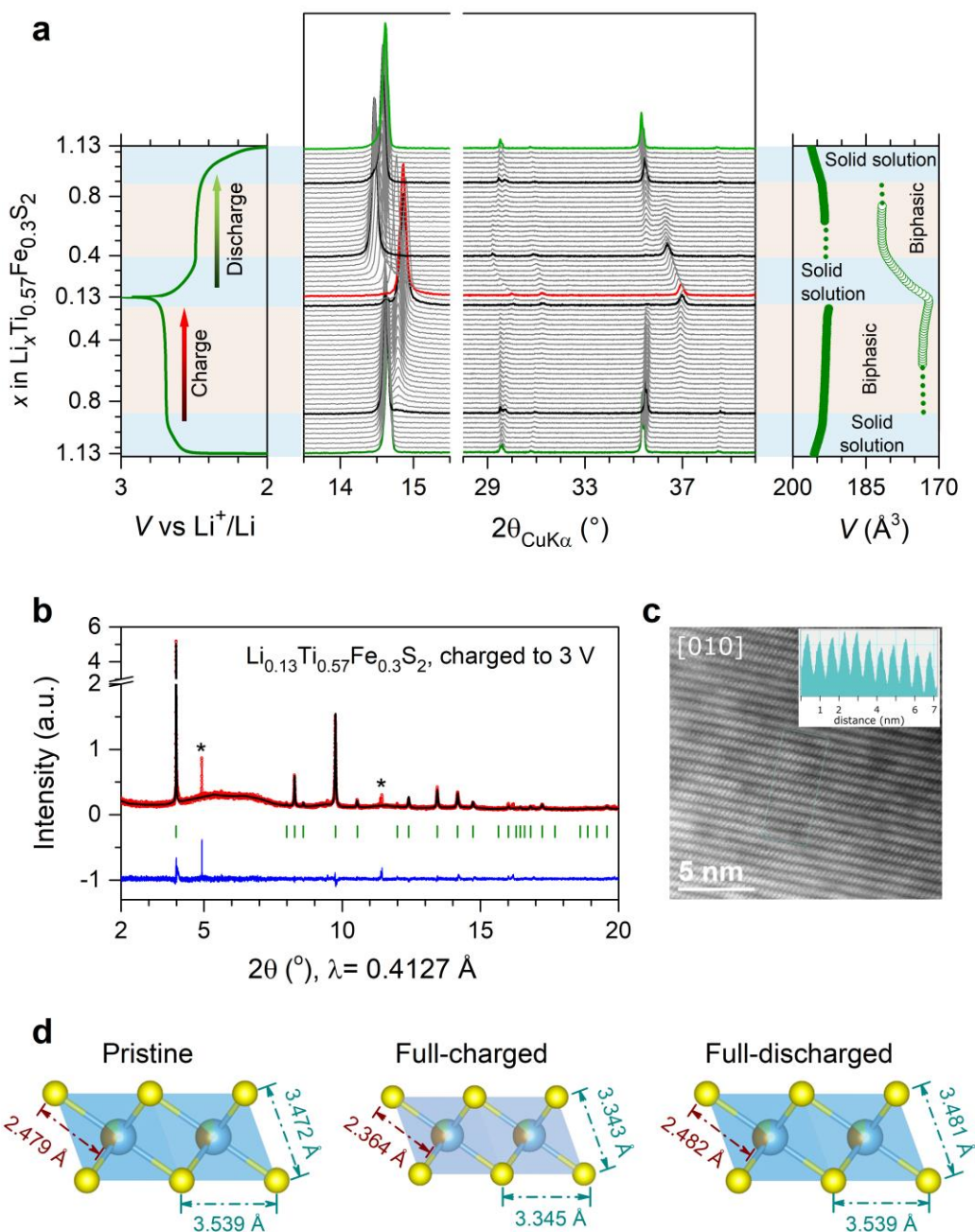


**Figure 4. Structural evolution upon Li (de)intercalation.** (a) Evolution of the *in situ* XRD patterns in the first cycle of a  $\text{Li}_{1.13}\text{Ti}_{0.57}\text{Fe}_{0.3}\text{S}_2$  /Li half-cell at a rate of C/20. The left panel shows the corresponding voltage profile and the right panel shows the evolution of the unit cell volume ( $V$ ), as obtained from the Rietveld refinements of the XRD patterns. Note that the dotted lines represent extrapolations, where the XRD patterns could not be refined because of poor intensity of the peaks. (b-c) Rietveld refinement of the SXR patterns (b) and the HAADF-STEM image (c) of the full-charged phase. The peaks denoted by \* in (b) show minor  $\text{Li}_2\text{TiO}_3$  impurity. The inset in (c) shows the HAADF intensity profile. (d) The bond-lengths observed in the pristine, full-charged and full-discharged phase (as obtained from the Rietveld refinement of the corresponding SXR patterns).

To grasp some insights on the charge compensation mechanism, the cationic  $\text{Fe}^{2+/3+}$  redox process was probed by *operando* Mössbauer spectroscopy using an electrochemical cell designed in-house.<sup>52</sup> Spectra were collected while charging and discharging a  $\text{Li}_{1.13}\text{Ti}_{0.57}\text{Fe}_{0.3}\text{S}_2/\text{Li}$  cell at a rate of C/70 (Figure 5). The Mössbauer spectra for pristine  $\text{Li}_{1.13}\text{Ti}_{0.57}\text{Fe}_{0.3}\text{S}_2$ , that can neatly be fitted with four doublets (see Table S5), highlights the presence of a distribution of high-spin (HS)  $\text{Fe}^{2+}$ , as already encountered for FeS and various other iron (II)-based sulfides.<sup>53,54</sup> The necessity of four doublets is simply due to different local arrangements of intermixed Ti/Li/Fe cations around a given Fe site. The evolution of the spectra obtained during *in situ* cycling is shown as a contour plot in Figure 5b, with the spectra analyzed using principal component analysis (PCA), as described in Supplementary Note S1. All measured spectra could be adequately fitted as linear-combinations of three reconstructed spectral components. As expected, the first component (*Comp. 1*) is identical to the pristine material's spectrum. The *Comp. 2* can be fitted using at least two doublets, see Figure 4a and Table S5. The major one (90%) has an isomer shift of 0.48 mm/s which stands between what is expected for HS  $\text{Fe}^{2+}$  and HS  $\text{Fe}^{3+}$ , alike what has been seen in  $\text{Fe}_3\text{S}_4$  and  $\text{FeV}_2\text{S}_4$ .<sup>53</sup> The second doublet with a 10 % contribution to the overall spectrum is indicative of the HS- $\text{Fe}^{3+}$  signature, as seen in  $\text{NaFeS}_2$ .<sup>53</sup> Overall, the average oxidation state of *Comp. 2* is higher than  $\text{Fe}^{2+}$  but not fully reaching  $\text{Fe}^{3+}$ . Note that *Comp. 2* reaches its maximum around  $x_{\text{Li}} = \sim 0.93$ , just before the voltage plateau. During the plateau, the *Comp. 2* converts progressively to the *Comp. 3* (fully-charged, 3 V), as shown in Figure 4c, in which can be fitted as low-spin  $\text{Fe}^{3+}$  state in agreement with previous reports (Figure 4a and Table S5).<sup>40</sup> On discharge, the evolution of the components is reversed, except for a much lower contribution from the *Comp. 2* (Figure 4a). This is fully consistent with the path dependence observed above with XRD. Overall, these data indicate the progressive oxidation of  $\text{Fe}^{2+}$  to  $\text{Fe}^{3+}$  on charge and its full reduction back to  $\text{Fe}^{2+}$  on discharge.

Furthermore, Fe  $L_{2,3}$ -edge X-ray absorption near edge structure (XANES) spectra were taken to confirm the participation of Fe and are shown in Figure S6b. The spectra for the pristine material is similar to that of FeS confirming the presence of  $\text{Fe}^{2+}$ .<sup>55,56</sup> It enlists two main peaks corresponding to  $2p_{3/2} \rightarrow 3d$  ( $L_3$ ) and  $2p_{1/2} \rightarrow 3d$  ( $L_2$ ) transitions. These peaks shift to higher energy upon charge indicating gradual conversion to  $\text{Fe}^{3+}$ . After discharge, the Fe  $L_{2,3}$  edge is restored completely. The position and shifts of the Fe  $L_{2,3}$ -edge observed upon oxidation are consistent with observations of S-containing species with  $\text{Fe}^{2+}$  and  $\text{Fe}^{3+}$  in literature,<sup>57</sup> indicating consistency with conclusions from Mössbauer spectroscopy. The Ti  $L_{2,3}$ -edge XANES spectra were also recorded for the aforementioned samples (Figure S6c). As expected, the spectrum for pristine  $\text{Li}_{1.13}\text{Ti}_{0.57}\text{Fe}_{0.3}\text{S}_2$  is identical to that of  $\text{Ti}^{4+}\text{S}_2$ , confirming the formal oxidation state of Ti as 4+. <sup>58</sup> Moreover, no changes in the position of  $L_2$  and  $L_3$  peaks could be observed, irrespective of the sample state of charge, hence indicating the invariance of  $\text{Ti}^{4+}$  throughout the charge/discharge cycle.<sup>58</sup>

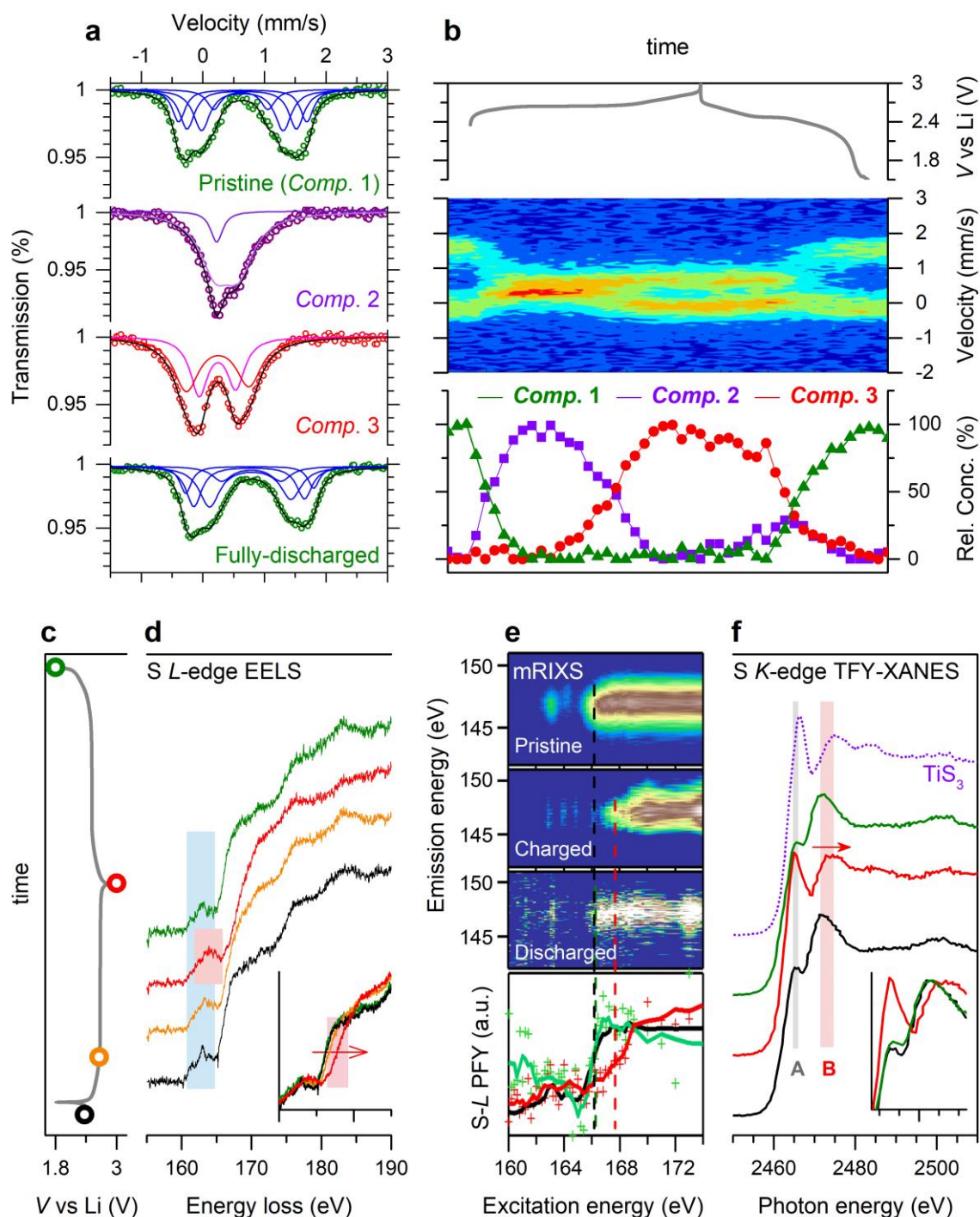


**Figure 5. Spectroscopic characterizations to identify the redox processes.** (a) Typical Mössbauer spectra and their deconvolution for the pristine (comp. 1), comp. 2, comp. 3 (fully charged) and the fully-discharged product. (b) Contour plot of evolution of the Mössbauer spectra collected during *in situ* cycling of a  $\text{Li}_{1.13}\text{Ti}_{0.57}\text{Fe}_{0.3}\text{S}_2/\text{Li}$  half-cell at a rate of C/70. For reference the voltage profile is shown in the top panel. The lowest panel shows the evolution of the reconstructed components during the cycling. (c-f) The EELS spectra of the S L-edge (d), mRIXS of the S L-edge with integrated PFY spectra on the bottom (e) and S K-edge XANES spectra (f) collected *ex situ* on the pristine (black curves), partially-charged (2.66 V, only EELS, orange curve), fully-charged (3 V, red curves) and fully-discharged phase (green curve) as shown in the voltage profile in (c).



To check the electrochemical activity of S within the  $\text{Li}_{1.13}\text{Ti}_{0.57}\text{Fe}_{0.3}\text{S}_2$  phase during the Li uptake and removal process, *ex situ* electron energy loss spectroscopy (EELS) spectra at the S  $L_{2,3}$  edge were collected (Figure 5d) for pristine, partially-charged (2.66 V, after removing  $\sim 0.16$  Li), fully-charged (3 V) and fully-discharged (1.8 V) samples. The spectra consist of a weak pre-edge and an intense broad edge feature that correspond to a series of transitions from the S  $2p$  core levels to unoccupied states.<sup>59</sup> The S  $L_{2,3}$  edge for the pristine material is similar to that of FeS indicating the predominance of  $\text{S}^{2-}$  state (Figure 5d and S7a).<sup>59</sup> It remains nearly alike for the partially charged sample (at 2.66 V) with the exception of minor alterations that could be ascribed to a probable decrease of the Ti/Fe–S bond covalency. In contrast, for the fully-charged sample (at 3 V), the S  $L_{2,3}$  rising-edge shifts by  $\sim 1.6$  eV towards higher energies and this is indicative of a partial oxidation of  $\text{S}^{2-}$ .<sup>55</sup> However the S  $L_{2,3}$  pre-edge does not show the typical peak splitting seen in pyrite- $\text{FeS}_2$  or elemental  $\text{S}^0$  (Figure S7b).<sup>56</sup> Lastly, it is worth mentioning that the initial shape as well as the energy of the rising-edge of the S  $L_{2,3}$  edge are fully recovered towards the end of the discharge, further indicative of the reversibility of the sulfur redox process.

To complement the EELS data that were collected locally on individual electrode particles (see Methods), we further probed the S  $L$ -edge by soft X-ray absorption spectroscopy (sXAS) performed in fluorescence mode which provides bulk-sensitive information about sulfur redox activity. However, direct measurements of the electrodes on the S  $L$ -edge through conventional sXAS turned out to be challenging, because of interfering background signals from the carbon present in the electrodes which contributes an overwhelming background through 2nd order harmonic around 140 eV, right below the S- $L$  signals around 160 eV (Figure S7c,d). We could successfully distinguish the S signals from the strong C background, by employing high-efficiency mapping of resonant inelastic X-ray scattering (mRIXS), see Methods and Figure S7e for details. This advanced technique, which has emerged as a seminal technique for detecting oxygen redox, further resolves the emitted photon energy, called emission energy, after each sXAS excitation process.<sup>60</sup> Figure 5e displays these S- $L$  mRIXS signals collected from the pristine, fully-charged, and fully-discharged electrodes. The integration of all the signals within the emission energy range (142 - 151 eV) provides the partial fluorescence yield (PFY) signals of the clean S- $L$  sXAS, as summarized in the bottom panel. The pristine  $\text{Li}_{1.13}\text{Ti}_{0.57}\text{Fe}_{0.3}\text{S}_2$  without carbon additive displays the strongest S- $L$  features. The relatively sharp features in mRIXS at 163 and 164.1 eV excitation energies correspond well with the pre-edge peaks observed in EELS. The sharp features suggest these are dominated by the localized TM  $3d$  character that is hybridized with S orbitals.<sup>59</sup> At higher excitation energy, the continuous band-like feature corresponds to the intrinsic sulfur states hybridized with TM  $4s/4p$  orbitals. It is clear that the leading edge of these sulfur band-like feature shifts towards high energy for over 1.2 eV in the full charged phase, in complete agreement with EELS and indicating the oxidation of sulfur states. Furthermore, the leading edge position completely recovers after discharge, suggesting a reversible redox reaction of the sulfur.

S  $K$ -edge XANES spectra were equally collected for the aforementioned samples (except partially charged) and they are reported in Figure 5e. The spectrum presents two main regions. The pre-edge feature, below 2471 eV, arises generally from unoccupied S  $3p$ /TM  $3d$  hybridized states. Their position and intensity depend on their occupancy, the relative contribution of S and TM, and their position with respect to the core level, thus being a general measure of covalence of the TM-S bond.<sup>61</sup> Above this energy, the signals correspond to transitions to higher states, such as S  $3p$ /TM  $4s$ ,  $p$  or those involving S  $4p$ , and the photoionization of S atoms, involving complete ejection of the core electron to the continuum. Therefore, the position of the absorption threshold is strongly dependent on the effective nuclear charge ( $Z_{\text{eff}}$ ) on S,<sup>61</sup>

being a measure of redox transitions at the ligands. The spectra for pristine  $\text{Li}_{1.13}\text{Ti}_{0.57}\text{Fe}_{0.3}\text{S}_2$  consists in a weak pre-edge at  $\sim 2465$  eV (denoted as **A**) and a broad edge jump (denoted as **B**) located at  $\sim 2472$  eV similar to what is observed in amorphous rocksalt  $\text{Li}_2\text{TiS}_3$  and hence characteristic of  $\text{S}^{2-}$ .<sup>48</sup> For the fully charged state ( $\sim \text{Li}_{0.1}\text{Ti}_{0.57}\text{Fe}_{0.3}\text{S}_2$ ), the spectrum (red curve in Figure 5e) undergoes notable changes with an increase in amplitude of the pre-edge **A** and a  $\sim 1.2$  eV shift of the **B** edge towards higher energy, and bears resemblance to  $\text{TiS}_3$  (dashed purple curve).<sup>62</sup> Similarly, the opposite shift in the edge **B** is observed during re-lithiation, as was reported for  $\text{TiS}_3$ , and  $\text{VS}_4$ .<sup>36,63</sup> The 1.2 eV shift in **B** is therefore a clear indication of the oxidation of  $\text{S}^{2-}$  into  $\text{S}^{n-}$ ,  $n < 2$ . Similarly, the increase in intensity of pre-edge **A** is indicative of the increase in density of unoccupied states just above the Fermi level with an S character, in agreement with the expectation that the redox change is compensated by S  $3p/\text{Fe } 3d$  electrons. The shift of the main absorption edge also suggests that this compensation, and the resulting states, have a significant S character. This unambiguously confirms the participation of S in the overall electrochemical activity of  $\text{Li}_{1.13}\text{Ti}_{0.57}\text{Fe}_{0.3}\text{S}_2$  together with its reversibility since the S  $K$ -edge XANES spectra of the fully-discharged and pristine samples nearly superimpose (Figure S6d).

To confirm the above observations S  $2p$  core X-ray photoelectron spectroscopy (XPS) spectra were also taken and are shown in Figure S6e. Clear variations of the spectra are observed upon charging-discharging the samples. The S  $2p_{3/2-1/2}$  XPS core spectrum can be fitted with a single doublet (160.7 - 161.9 eV) attributable to  $\text{S}^{2-}$  for the pristine material, as in the  $\text{TiS}_2$  reference.<sup>64</sup> As the sample gets oxidized, the spectrum markedly changes, with namely the appearance of one extra doublet at higher binding energies (161.8 - 163.0 eV), which is indicative of the presence of oxidized  $\text{S}^{n-}$  ( $n < 2$ ), in light of early previous studies on  $\text{TiS}_3$  that is well-known to contain partially oxidized sulfur.<sup>32,64</sup> On discharge, the XPS spectrum is almost restored to the pristine-like state, confirming the reversibility of the anionic redox process.

At this stage, mindful of the strong involvement of anionic redox in the charge compensation mechanism of  $\text{Li}_{1.13}\text{Ti}_{0.57}\text{Fe}_{0.3}\text{S}_2$ , the next legitimate question pertains to the practicability of anionic redox in sulfides. Using these newly designed Li-rich sulfides as model compounds, we investigated whether some of the practical issues (large voltage hysteresis, sluggish kinetics and gradual voltage fade) that have so far plagued the commercialization of analogous Li-rich layered oxides showing anionic redox activity<sup>12,6</sup>, still persist when oxygen is replaced by sulfur. To assess the practical figures of merit in Li-rich sulfides, we first performed a galvanostatic intermittent titration technique (GITT) experiment (Figure 6a) after initial seven cycles to stabilize the voltage profile.  $\text{Li}_{1.13}\text{Ti}_{0.57}\text{Fe}_{0.3}\text{S}_2$  shows the disappearance of voltage hysteresis in the open-circuit voltage (OCV) throughout the cycle (only  $\sim 30$  mV gap remains after just 30 mins of relaxation). This is a significantly better scenario than in Li-rich NMC ( $\text{Li}_{1.2}\text{Ni}_{0.13}\text{Mn}_{0.54}\text{Co}_{0.13}\text{O}_2$ ), where a severe OCV hysteresis up to 300 mV has been reported and further shown to be associated with oxygen redox (Figure 6b).<sup>14</sup> This performance is also better than the  $\sim 100$  mV OCV hysteresis in  $4d$  metal-based  $\text{Li}_2\text{Ru}_{0.75}\text{Sn}_{0.25}\text{O}_3$  and approaches the favorable hysteresis-free situation experienced in  $5d$  metal-based  $\beta\text{-Li}_2\text{IrO}_3$ .<sup>13,16</sup> This observation clearly highlights that voltage hysteresis can be effectively mitigated by tuning the ligand, and not just by choosing appropriate transition metals. The hysteresis was further studied by progressive opening of voltage-windows during charge in subsequent cycles and the voltage profiles are summarized in Figure 6c. Increasing the voltage cut-off does not lead to any noticeable increase in voltage hysteresis. This contrasts with similar experiments on Li-rich NMC showing an onset of large hysteresis upon full charging accompanied with lowering of the discharge potential around mid-SoCs (Figure S8a). Furthermore, the corresponding  $dQ/dV$  curves (in the inset, Figure 6c) reveal that irrespective of upper cut-off of charging voltage, in discharge the oxidative capacities are mostly recovered at  $\sim 2.5$  V, therefore not triggering any voltage hysteresis. This is quite contrary to Li-rich NMC, where oxidative capacities obtained

from anionic redox (i.e., charging above ~4.1 V) are only recovered partially at similar voltage upon discharge (down to ~4 V). Further discharge to a lower voltage (below ~3.6 V) is necessary to regain the remaining capacity, as the reduction of the oxidized  $O^{n-}$  species is split between high and low voltages, causing a large voltage hysteresis (Figure S8b).<sup>14</sup>

Concerning the next issue of kinetics, we have previously shown how oxygen redox displays sluggish kinetics.<sup>13,14</sup> Hence, to check the same in sulfides, cell resistance was deduced from the voltage drop during the first 10 s of the relaxation steps of the GITT experiment (Figure 6b). As revealed for  $Li_{1.13}Ti_{0.57}Fe_{0.3}S_2$ , the electrochemical resistance remains quite low throughout the whole cycle (Figure 6d). Whereas for Li-rich NMC, the resistance is significantly larger at all SoCs and increases at low and high SoCs, which corresponds to the regions involving oxygen redox.<sup>14</sup> Furthermore, electrochemical impedance spectra (EIS) were collected at different SoCs of  $Li_{1.13}Ti_{0.57}Fe_{0.3}S_2$ , after each relaxation step during the GITT experiment and the evolution of the EIS Nyquist plots is shown in Figure S9a,b. The charge-transfer resistance, located in the mid-frequency regime of the spectra (characteristic frequency around 10 to 1 Hz), remains very small and nearly constant throughout the cycle, irrespective of whether it is cationic or anionic redox regime, as opposed to Li-rich oxides where the resistance builds up drastically with deeper oxidation of oxygen.<sup>12,14</sup> This clearly highlights the positive attribute of Li-rich sulfides concerning kinetics. The fast kinetics was further confirmed with  $Li_1Ti_{0.5}Fe_{0.5}S_2$  ( $y = 0.5$ ) composition, which shows similar charge transfer resistance and consequently similar cycling and rate performance (Figure S9c,d), despite having a higher proportion of cationic redox capacity. Lastly, regarding the critical issue of voltage fade, we found that it still afflicts Li-rich sulfides, though to a much lower extent, as shown in Figure 6e. The voltage fade for  $Li_{1.13}Ti_{0.57}Fe_{0.3}S_2$  can be divided in two regimes, starting first with a well-pronounced decrease from 2<sup>nd</sup> cycle to the 7<sup>th</sup> (a drop of ~35 mV) followed by a stabilization afterwards to reach an overall drop of ~40 mV after 60 cycles (the maximum we have cycled). This again positively contrasts with Li-rich NMC that shows a nearly continuous voltage fade upon cycling with an accumulated drop of ~150 mV after 60 cycles. Overall, moving from oxygen to sulfur as the ligand turns out to be a correct strategy to partially mitigate the practical bottlenecks of anionic redox. However, we need to keep in mind that this comes at the expense of the overall energy density (Figure 6f) because of lower potential and higher molecular weight of sulfur. A compromise could consist in combining the energy advantage of oxygen redox with the practicability of sulfur redox. This task is not trivial bearing in mind the experienced difficulty in preparing 3d-metal-based oxysulfides.



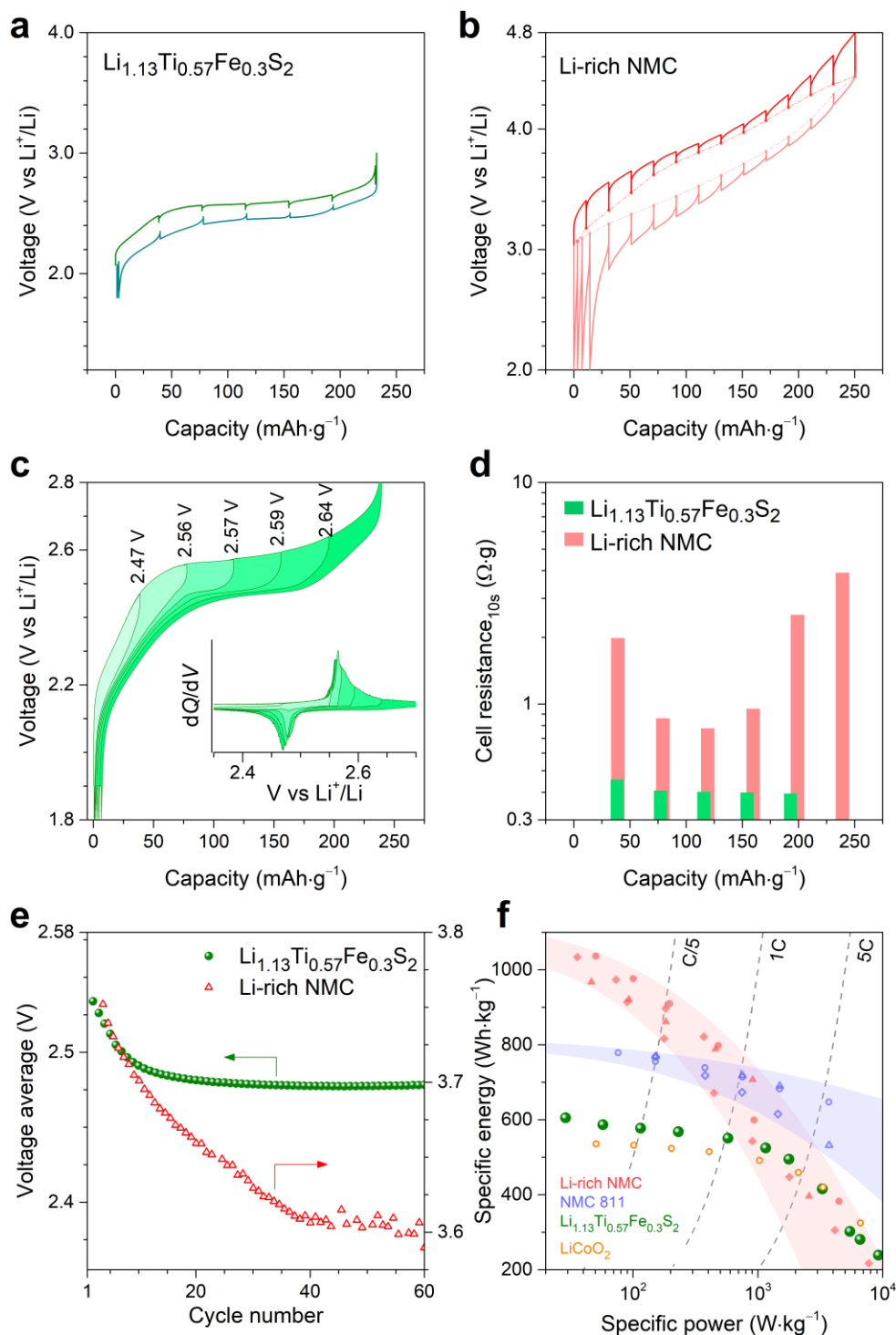


**Figure 6. Li-rich layered sulfide as a model material to study the practicability of anionic redox.** (a) Voltage profile of  $\text{Li}_{1.13}\text{Ti}_{0.57}\text{Fe}_{0.3}\text{S}_2$  in a two-electrode cell in the 8<sup>th</sup> cycle, recorded with a GITT protocol (C/5 rate with 30 min rests for equilibration). (b) Voltage profile of Li-rich NMC ( $\text{Li}_{1.2}\text{Ni}_{0.13}\text{Mn}_{0.54}\text{Co}_{0.13}\text{O}_2$ ) in a three-electrode cell in the 4<sup>th</sup> cycle, recorded with a GITT protocol (40  $\text{mA}\cdot\text{g}^{-1}$  pulses with 4 h rests for equilibration). (c) Voltage profiles obtained from the charge-window opening experiment (starting from 8<sup>th</sup> cycle). Inset shows the corresponding  $dQ/dV$  profiles. (d) Cell's electrochemical resistance (during charging) estimated simply by Ohm's law from the voltage drop in first 10 s of rest from the previous GITT experiment in (a). (e) Average voltage during long cycling of  $\text{Li}_{1.13}\text{Ti}_{0.57}\text{Fe}_{0.3}\text{S}_2$  and Li-rich NMC in Li-half cells. In each cycle, the average voltage is defined as the

mean of the average charge and discharge voltages that and was calculated by dividing the energy with the capacity obtained. (f) Ragone plots of  $\text{Li}_{1.13}\text{Ti}_{0.57}\text{Fe}_{0.3}\text{S}_2$  and comparison with Li-rich NMC and Li-stoichiometric NMC ( $\text{LiNi}_{0.8}\text{Mn}_{0.1}\text{Co}_{0.1}\text{O}_2$ ). Only values at material-level are considered and values for the NMC-811 and the Li-rich NMC are adapted from *Reference*<sup>12</sup>.  $\text{LiCoO}_2$  is also included in the comparison and the Li-rich layered sulfide appears at par with it.

## Discussion

We have shown the feasibility, by partially substituting  $\text{Ti}^{4+}/\text{Li}^+$  belonging in the metal layers of  $\text{Li}_{1.33}\text{Ti}_{0.67}\text{S}_3$  (commonly written  $\text{Li}_2\text{TiS}_3$ ) with  $\text{Fe}^{2+}$ , to produce  $\text{Li}_{1.33-2y/3}\text{Ti}_{0.67-y/3}\text{Fe}_y\text{S}_2$  phases showing electrochemical activity due to cumulated cationic ( $\text{Fe}^{2+/3+}$ ) and anionic ( $\text{S}^{2-} / \text{S}^{n-}$ ,  $n < 2$ ) redox processes. Alike the Li-rich layered oxides having  $d^0$  metals ( $\text{Li}_2\text{TiO}_3$ , etc...), we found the feasibility to trigger Li electrochemical activity in Li-rich layered sulfides having  $d^0$  metals by the injection of metal substituents. This does not come as a total surprise as such metal substitution modifies the  $U$  over  $\Delta$  competition, so that it falls within the domain to trigger reversible anionic redox activity as established from theoretical calculations.<sup>41</sup> The anionic redox activity upon oxidation was spectroscopically confirmed in  $\text{Li}_{1.13}\text{Ti}_{0.57}\text{Fe}_{0.3}\text{S}_2$  via clear energy shifts in the S  $L_{2,3}$ -edge EELS and XANES spectra as well as the onset of a doublet signal in the S  $2p_{3/2-1/2}$  XPS core spectra. Structure-wise on the other hand, our XRD and EELS evidence did not suggest the local formation of very short S–S dimers (like in pyrites), but more investigations focusing on the local structure are needed to unequivocally rule this out. For comparing with oxides, let's recall that the XPS fingerprint of anionic redox activity in oxides was also the appearance of a new component at slightly higher binding energy (531.5 eV) in the O  $1s$  XPS core spectra that we assigned to  $\text{O}^{n-}$  ( $n < 2$ ).<sup>14–16</sup> Interestingly, the binding energy of this component was independent of the structure and composition as seen in various Li-rich oxides that show anionic redox activity, with or without evidences of O–O shortening. This observation indicates that although XPS features have been widely used as the spectroscopic signature of the anionic redox activity in various materials, caution has to be exercised when interpreting XPS spectra.

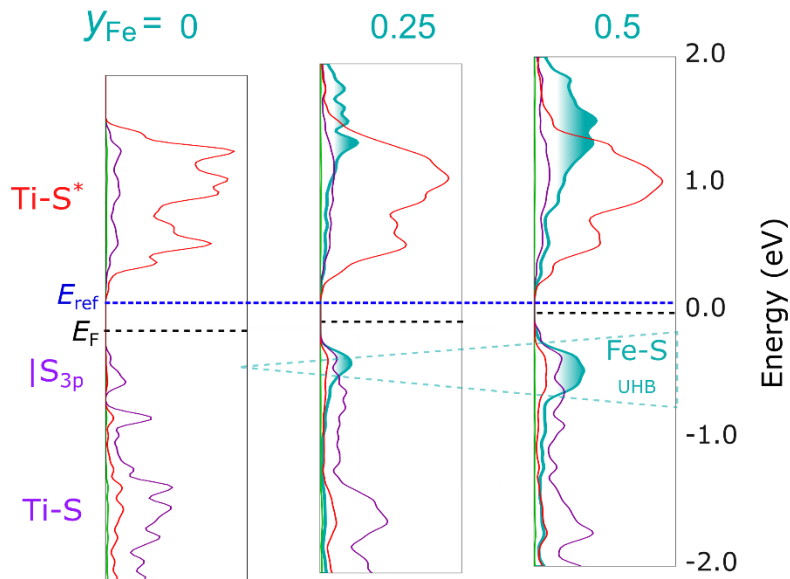
Besides, we found that  $\text{Li}_{1.13}\text{Ti}_{0.57}\text{Fe}_{0.3}\text{S}_2$  can deliver capacities as high as  $245 \text{ mAh} \cdot \text{g}^{-1}$  with a near-zero irreversible capacity during the first cycle as compared to  $\sim 0.2 \text{ Li}$  for Li-rich  $3d$  metal-based oxides (Figure S8c,d). This is consistent not only with the absence of cationic migration in sulfides, in contrast to some of the analogous oxides, but also with less severe changes observed between the first charge-discharge voltage profiles in  $\text{Li}_{1.13}\text{Ti}_{0.57}\text{Fe}_{0.3}\text{S}_2$  as opposed to Li-rich NMCs that show a staircase charging curve drastically changing to a S-shaped discharging curve. Lastly, part of the initial irreversibility in oxides is associated to a small amount of oxygen release from the surface, either directly as  $\text{O}_2$  gas or indirectly by reacting with the electrolyte.<sup>3,65</sup> This is quite unlikely to occur with S which is a softer element as compared to O, therefore showing less reactivity and greater stability for the same degree of electrochemical oxidation.

We noted in the  $dQ/dV$  profile (recall Figure 3b) a systematic shift to lower potentials of the peaks corresponding to concomitant cationic and anionic redox processes with increasing Fe-content in  $\text{Li}_{1.33-2y/3}\text{Ti}_{0.67-y/3}\text{Fe}_y\text{S}_2$ , while for instance the position of the peaks was found to remain independent of Sn substitution in the  $\text{Li}_2\text{Ru}_{1-y}\text{Sn}_y\text{O}_3$  series showing well-decoupled cationic and anionic redox.<sup>15</sup> To understand this behaviour, we calculated the spin-projected density of states (pDOS) for  $y = 0, 0.25$  and  $0.5$  (these compositions were chosen for ease of computation, see Methods) and plotted in Figure 7a. The electronic structure of the parent  $\text{Li}_{1.33}\text{Ti}_{0.67}\text{S}_2$  displays a charge transfer gap between the empty Ti  $d$  band (in red), split by the crystal field, and the S band (in purple) formed of non-bonding S  $3p$  states (denoted as  $|\text{S}_{3p}\rangle$ ) that lies above the Ti–S bonding states.  $\text{Fe}^{2+}$  substitution leads to the introduction of a partially filled  $d$  band (having six electrons), which is split by  $d$ - $d$  Coulomb repulsion (introduced by a correction term  $U = 1.9 \text{ eV}$ ) into a deep-lying Lower Hubbard band (LHB), with five spin-up electrons, and an Upper Hubbard Band (UHB)

with one spin-down electron. This is consistent with the experimentally observed HS  $\text{Fe}^{2+}$  from Mössbauer spectroscopy. The occupied states of the UHB lie above the  $|\text{S}_{3p}$  states. As the Fe content increases, the number of these UHB states increases. If we take as a reference the energy ( $E_{\text{ref}}$ ) of states that are not expected to be directly affected by the Fe substitution, such as either the  $\text{Ti-}t_{2g}^*$  that is close to the Fermi level (Figure 7a) or the S 3s core levels that are non-bonding and very deep in energy (see Figure S10a), we observe that the highest occupied states are rising in energy with Fe content as indicated by the raising of the Fermi level. This explains the experimental observation of voltage decrease with gradual Fe introduction.

Next we asked whether the experimentally observed electronic and structural changes upon Li removal could be supported by monitoring the evolution of pDOS and the corresponding theoretical S–S distances. This is answered by calculating the pDOS of  $\text{Li}_x\text{Ti}_{0.58}\text{Fe}_{0.25}\text{S}_2$  ( $1.17 > x_{\text{Li}} > 0.83$ ) that is summarized in Figure 7b. At the beginning of charge ( $1.17 > x_{\text{Li}} > 0.83$ ), the depletion of the Fe-UHB near the Fermi level indicates that Fe gets oxidized, while the average S–S distance remains unaffected and thus confirming that S acts as a spectator. This situation drastically changes upon further oxidation ( $0.83 > x_{\text{Li}} > 0.17$ ) where the pDOS indicates the depletion of the S band near the Fermi level, which implies S undergoes partial oxidation. Over this composition range, the small decrease in some of the calculated S–S distances (marked in purple background in the histograms) and the progressive closing of the band gap suggests that the holes are delocalized over the S network through Fe–S interaction. The participation of S to the states right above the Fermi level significantly increased upon oxidation, consistent with the increase in pre-edge intensity observed by S K-edge XAS (Figure 5f).

a) Increasing Fe content in  $\text{Li}_{1.33-2y/3}\text{Ti}_{0.67-y/3}\text{Fe}_y\text{S}_2$



b) Decreasing Li content in  $\text{Li}_x\text{Ti}_{0.58}\text{Fe}_{0.25}\text{S}_2$

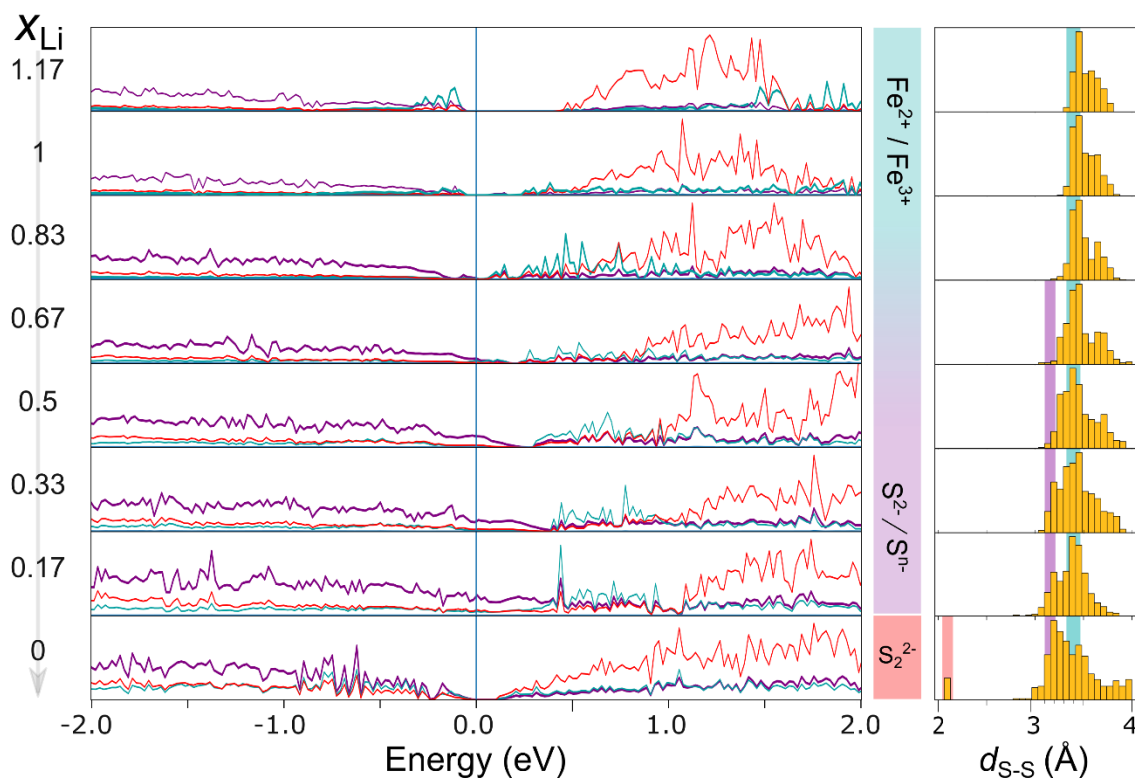


**Figure 7. Correlating the experimental observations in  $\text{Li}_{1.33-2y/3}\text{Ti}_{0.67-y/3}\text{Fe}_y\text{S}_2$  with theoretical calculations.** (a) Evolution of pDOS with increasing Fe content. Li, Ti, Fe and S contributions to bands are colored in light green, red, cyan and purple, respectively (b) Evolution of pDOS of  $\text{Li}_{1.17}\text{Ti}_{0.58}\text{Fe}_{0.25}\text{S}_2$  with Li-removal. The panel in middle indicates the deduced redox processes. The corresponding theoretically obtained S-S distances are shown in the histograms at right. The distances were chosen using a distance cut-off of 4 Å, without renormalization.

At high states of charge, the top of the highly dispersed sulfur band gets raised above the bottom of the empty Fe-UHB leading to electronic instability. This scenario triggers, if we simulate complete Li removal ( $x_{\text{Li}} \sim 0$ ), a reorganization of the network through the formation of true S–S dimers with a calculated bond length of  $\sim 2.1$  Å (red background in the histogram). However, experimentally, full Li depletion is not observed since our fully oxidized sample still contains 0.13 Li<sup>+</sup> ( $\sim \text{Li}_{0.13}\text{Ti}_{0.57}\text{Fe}_{0.3}\text{S}_2$ ). In short, the participation of S in the redox process could unambiguously be confirmed theoretically, hence explaining the measured shortening of the S–S distances. However, the predicted dimerization at full charge could not be confirmed experimentally because the fully delithiated phase was not obtained electrochemically. This finding probably explains the excellent cycling reversibility of  $\text{Li}_{1.33-2y/3}\text{Ti}_{0.67-y/3}\text{Fe}_y\text{S}_2$ , as opposed to  $\text{TiS}_3$ , where the cleavage of the S–S dimers leads to huge rearrangements of the crystal structure, resulting to rapid capacity fading with cycling.<sup>30–32</sup> Nevertheless, the question of  $(\text{S}_2)^{2-}$  vs.  $\text{S}^{n-}$  ( $n < 2$ ) upon complete delithiation remains to be fully elucidated, which will likely trigger more detailed characterizations and theoretical calculations on various sulfide materials in the future.

In summary, a new class of Li-rich layered sulfides  $\text{Li}_{1.33-2y/3}\text{Ti}_{0.67-y/3}\text{Fe}_y\text{S}_2$  have been designed and studied for their electrochemical behaviour as cathode materials. Within this series, the phase  $\text{Li}_{1.13}\text{Ti}_{0.57}\text{Fe}_{0.3}\text{S}_2$  offers the largest reversible capacity (245 mAh·g<sup>-1</sup>) and we have shown, via complementary Mössbauer, XANES, EELS, mRIXS and XPS spectroscopies, that this capacity mainly originates from sulfur redox besides the cationic redox of Fe. When benchmarking against Li-rich NMCs, this phase presents several positive attributes such as (i) a nearly zero irreversible capacity during the initial cycle, (ii) an overall voltage fade as low as 40 mV even after 60 cycles and (iii) low voltage hysteresis (35 mV), along with fast kinetics, as compared to Li-rich NMC showing an irreversibility of  $\sim 0.2$  Li, a voltage fade of 150 mV and a hysteresis of 300 mV besides sluggish kinetics. Energy-wise, these Li-rich layered sulfide positive electrodes display a specific energy of  $\sim 600$  Wh·kg<sup>-1</sup> at the material-level while being composed of earth-abundant elements (3d metals only). This is much lower than the  $\sim 1000$  Wh·kg<sup>-1</sup> obtained for Li-rich NMC and thus they may not offer any real-world competitiveness against oxide electrodes furthermore due to their low operating potential as well as the practical issues with the handling of sulfides. Nevertheless, we believe that they could serve as excellent ‘model’ electrodes to study the general properties of anionic redox chemistry and in exploring kinetics, especially via the realization of S-based solid-state batteries that can enable playing with temperature as an extra dimension. Both low hysteresis and structural integrity upon Li (de)intercalation are promising assets to design next-generation cathodes provided we can overcome the energy density penalty pertaining to the use of sulfur as a ligand. Preparing 3d-metal oxysulfides is an option if we ever overcome their synthesis difficulties. The door is wide-open for chemists to take forward this new dimension of exploring the effect of the ligand in enhancing the holistic performances of anionic redox in search for practical high-energy batteries.

## 496 Experimental Section

497 **Synthesis.**  $\text{Li}_{1.33-2y/3}\text{Ti}_{0.67-y/3}\text{Fe}_y\text{S}_2$  samples were prepared by solid-state reaction of stoichiometric amounts of  $\text{Li}_2\text{S}$  (Alfa Aesar,  
498 99.9%),  $\text{TiS}_2$  (Sigma Aldrich, 99.9%) and  $\text{FeS}$  (Alfa Aesar, 99%). Homogeneously mixed and hand-grinded precursor powders  
499 were filled in quartz tubes in an Ar-filled glovebox followed by sealing the tubes under vacuum ( $\sim 10^{-5}$  mbar). The sealed tubes  
500 were subsequently annealed at 750 °C for 36 h followed by quenching in water. The as-prepared samples were collected inside a  
501 glovebox and hand-grinded prior to further use. In the whole process, air contact was avoided and subsequent processing was done  
502 in an Ar-filled glovebox.  $\text{TiS}_3$ , used as a reference for XAS, was prepared similarly, by reacting  $\text{TiS}_2$  and elemental S (15 wt%  
503 extra), in a vacuum sealed quartz tube at 550 °C, followed by cooling slowly.

504 **Structural Characterization.** Synchrotron X-ray powder diffraction (SXRD) patterns were collected at the 11-BM beamline of  
505 the Advanced Photon Source (APS), Argonne National Laboratory. All SXRD data were collected in transmission mode with  $\lambda =$   
506 0.4127 Å, with the powder sealed in a quartz capillary of 0.7 mm diameter. Operando and *in situ* X-ray powder diffraction (XRD)  
507 was performed in an airtight electrochemical cell equipped with a Be window. XRD patterns were recorded in reflection mode in  
508 Bragg–Brentano geometry using a Bruker D8 Advance diffractometer equipped with a  $\text{Cu-K}\alpha$  X-ray source ( $\lambda_1 = 1.54056$  Å,  $\lambda_2 =$   
509 1.54439 Å) and a LynxEye detector. The refinements of the patterns were done using the Rietveld method<sup>66</sup> as implemented in the  
510 FullProf program<sup>67</sup>.

511 **Electrochemical characterization.**  $\text{Li}_{1.33-2y/3}\text{Ti}_{0.67-y/3}\text{Fe}_y\text{S}_2$  samples were cycled in galvanostatic mode in Li half-cells assembled  
512 in Swagelok-type cells. The cathode materials were mixed with 20 wt% conductive carbon Super-P by hand-grinding for 5 min  
513 prior to cycling (Figure S2d inset). LP30 (1M  $\text{LiPF}_6$  in ethylene carbonate/dimethyl carbonate in 1:1 weight ratio) was used as the  
514 electrolyte and was soaked in a Whatman GF/D borosilicate glass fiber membrane that was used as separator. Typical loadings of  
515 10 mg of active materials were used and metallic Li was used as the negative electrode. The cells were assembled in an Ar-filled  
516 glovebox and were cycled at a C/20 rate between 1.8 V and 3 V if not specified otherwise. Charged/discharged samples from the  
517 Swagelok cells were recovered for *ex situ* characterizations by disassembling the cells inside glovebox, rinsed thoroughly with  
518 anhydrous DMC and dried under vacuum. All electrochemical cycling and EIS measurements (in 10 mHz – 200 kHz frequency  
519 range applying a 10 mV sinusoidal wave) were performed with BioLogic potentiostats.

520 **Mössbauer spectroscopy.** Room-temperature  $^{57}\text{Fe}$  Mössbauer spectra were recorded in transmission geometry in the constant  
521 acceleration mode and with a  $^{57}\text{Co(Rh)}$  source with a nominal activity of 370 MBq. The velocity scale ( $\pm 4$  mms<sup>-1</sup>) was calibrated  
522 at room temperature with  $\alpha$ -Fe foil. The *in situ* cell was prepared with 32 mg.cm<sup>-2</sup> of active material mixed with 8 mg of carbon  
523 black. The hyperfine parameters IS (isomer shift) and QS (quadrupole splitting) were determined by fitting Lorentzian lines to the  
524 experimental data. The isomer shifts values are calculated with respect to that of  $\alpha$ -Fe standard at room temperature. The obtained  
525 operando spectra were fitted using a statistical method based on Principal Component Analysis (PCA). This approach is a  
526 chemometric factor analysis tool able to determine the minimal particular structures in multivariate spectral data sets. Once the  
527 number of principal components is determined by PCA, a Multivariate Curve Resolution-Alternating Least Squares (MCR-ALS)  
528 algorithm is used for the stepwise reconstruction of the pure spectral components which are necessary for interpreting the whole  
529 multiset of operando Mössbauer spectra.<sup>68</sup>

530 **Energy loss spectra (EELS).** The sample was prepared in an Ar-filled glove box by crushing the crystals in a mortar in DMC and  
531 depositing drops of the suspension onto holey carbon grids. The samples were transported to the transmission electron microscope  
532 (TEM) column while completely avoiding contact with air. High angle annular dark field scanning transmission electron microscopy  
533 (HAADF-STEM) images and EELS spectra were obtained with a FEI Titan G3 electron microscope operated at 120 kV and  
534 equipped with a monochromator and a Gatan Enfium ER spectrometer. Energy resolution measured by full width at half maximum  
535 of the zero loss peak is 0.15 eV.

536 **X-ray absorption spectroscopy (XAS).** S K-edge, Fe L-edge and Ti L-edge X-ray absorption near edge spectroscopy (XANES)  
537 measurements were performed at 4-ID-C beamline of APS at Argonne National Laboratory. Spectra were recorded simultaneously  
538 under both the total electron yield (TEY) mode from the sample photocurrent at  $\sim 10^{-9}$  Torr and total fluorescence yield (TFY) mode  
539 using a silicon drift diode detector at a spectral resolution of  $\sim 0.2$  eV, with a 2 s dwell time. The energy scales of the spectra were  
540 calibrated with the references of Mo metal, Fe metal and  $\text{SrTiO}_3$  measured simultaneously, for S, Fe and Ti edges, respectively.  
541 Both TEY and TFY spectra produces similar spectra, and hence only TFY spectra (more bulk sensitive) has been reported here.

542 **Soft X-ray absorption spectroscopy (sXAS) and mapping of resonant inelastic X-ray scattering (mRIXS).** The S L-edge sXAS  
543 and mRIXS experiments were performed in the iRIXS endstation of beamline 8.0.1 at the Advanced Light Source (ALS) of

Lawrence Berkeley National Laboratory.<sup>69</sup> The pristine powder and cycled electrodes were mounted in high purity Ar glove box and transferred into the experimental vacuum chamber through a home-made kit to avoid any air exposure. The experimental energy resolution of sXAS is better than 0.1 eV without considering the intrinsic core hole broadening (~0.2 eV). The energy resolution along the emission energy in mRIXS is about 0.2 eV,<sup>69</sup> which is sufficient for separating the intrinsic S-L signals from the strong C-K (2<sup>nd</sup> order) background that are different for about 10 eV. The X-ray exposure area on the samples were kept moving throughout the mRIXS experiments to avoid irradiation damage.

**X-ray photoemission spectroscopy (XPS).** XPS spectra were collected on a sample (analyzed area = 300×700 μm<sup>2</sup>) with a Kratos Axis Ultra spectrometer, using focused monochromatic Al Kα radiation ( $h\nu = 1.4866$  keV). The pressure in the analysis chamber was around  $5 \times 10^{-9}$  mbar. The binding energy scale was calibrated using the C 1s peak at 285.0 eV from the invariably present hydrocarbon contamination (for the pristine sample), and using the S<sup>2-</sup> position of the S 2p<sub>3/2</sub> at 160.7 eV for a better accuracy (for the other cycled samples). Peaks were recorded with constant pass energy of 20 eV. Core peaks were analyzed using a nonlinear Shirley-type background.<sup>70</sup> The peak positions and areas were optimized by a weighted least-squares fitting method using 70 % Gaussian, 30 % Lorentzian line shapes. Quantification was performed on the basis of Scofield's relative sensitivity factors.<sup>71</sup>

**Theoretical calculations.** Starting from a 221 supercell of Li<sub>2</sub>TiS<sub>3</sub> obtained from SXRD refinement, with honeycomb ordering of Li/Ti in the metallic layer, we achieved a composition of Li<sub>1.17</sub>Ti<sub>0.58</sub>Fe<sub>0.25</sub>S<sub>2</sub> (resp. Li<sub>1</sub>Ti<sub>0.5</sub>Fe<sub>0.5</sub>S<sub>2</sub>) by replacing 2 Li (resp. 4) and 1 Ti (resp. 2) atoms by Fe atoms. The atoms to replace were chosen to minimize the total Madelung energy of the final structure. To delithiate, we iteratively removed the Li atoms according to their Madelung energy (assuming integer oxidation state for every ion), using the Python Material Genome library.<sup>72</sup> For each Li content, structures were then relaxed using the Vienna Ab-Initio Simulation Package using ultra-soft PAW pseudo potentials and the Perdew-Burke-Ernzerhof functional with a generalized gradient approximation.<sup>73,74</sup> We added D3 correction to account for the van der Waals interaction<sup>75</sup> as well as a  $U_{\text{eff}} = 1.9$  eV to account for electron-electron interactions on Fe.<sup>76</sup> The forces on the atoms were converged to 10<sup>3</sup> eV Å<sup>-1</sup> with a plane-wave energy cut-off of 600 eV and a well converged set of Kpoints.

**Acknowledgements:** S.S. thanks the Réseau sur le Stockage Electrochimique de l'Energie (RS2E) for funding of the Ph.D. J.-M.T. acknowledges funding from the European Research Council (ERC) (FP/2014)/ERC Grant-Project 670116-ARPEMA. Use of the 11-BM mail service of the APS at Argonne National Laboratory was supported by the US Department of Energy under contract No. DE-AC02-06CH11357 and is gratefully acknowledged. The sXAS and mRIXS experiments at BL8.0.1 used resources of the Advanced Light Source, which is a DOE Office of Science User Facility under contract no. DE-AC02-05CH11231. The authors thank M. Saubanère & M-L. Doublet for fruitful discussions and the laboratory Chimie Théorique Methodes & Modélisation (CTMM) at the Institut Claude Gerhardt Montpellier (ICGM) for computational facilities.

## 576 References:

- 577 1. Blomgren, G. E. The Development and Future of Lithium Ion Batteries. *J. Electrochem. Soc.* **164**, A5019–A5025 (2017).
- 578 2. Schmuch, R., Wagner, R., Hörpel, G., Placke, T. & Winter, M. Performance and cost of materials for lithium-based rechargeable  
579 automotive batteries. *Nat. Energy* **3**, 267–278 (2018).
- 580 3. Luo, K. *et al.* Charge-compensation in 3d-transition-metal-oxide intercalation cathodes through the generation of localized electron holes  
581 on oxygen. *Nat. Chem.* **8**, 684–691 (2016).
- 582 4. Koga, H. *et al.* Reversible Oxygen Participation to the Redox Processes Revealed for Li 1.20 Mn 0.54 Co 0.13 Ni 0.13 O 2. *J. Electrochem.*  
583 *Soc.* **160**, A786–A792 (2013).
- 584 5. Yabuuchi, N. Solid-state Redox Reaction of Oxide Ions for Rechargeable Batteries. *Chem. Lett.* **46**, 412–422 (2017).
- 585 6. Seo, D.-H. *et al.* The structural and chemical origin of the oxygen redox activity in layered and cation-disordered Li-excess cathode  
586 materials. *Nat. Chem.* **8**, 692–697 (2016).
- 587 7. Saubanè, M., Mccalla, E., Tarascon, J.-M. & Doublet, M.-L. The intriguing question of anionic redox in high-energy density cathodes for  
588 Li-ion batteries. *Energy Environ. Sci.* **9**, 984 (2016).
- 589 8. Okubo, M. & Yamada, A. Molecular Orbital Principles of Oxygen-Redox Battery Electrodes. *ACS Appl. Mater. Interfaces* **9**, 36463–  
590 36472 (2017).
- 591 9. Yabuuchi, N. *et al.* Origin of stabilization and destabilization in solid-state redox reaction of oxide ions for lithium-ion batteries. *Nat.*  
592 *Commun.* **7**, 13814 (2016).
- 593 10. Maitra, U. *et al.* Oxygen redox chemistry without excess alkali-metal ions in Na 2/3 [Mg 0.28 Mn 0.72 ]O 2. *Nat. Chem.* **10**, 288–295  
594 (2018).
- 595 11. Mortemard de Boisse, B. *et al.* Highly Reversible Oxygen-Redox Chemistry at 4.1 V in Na  $_{4/7-x}$  [□  $_{1/7}$  Mn  $_{6/7}$ ]O  $_2$  (□: Mn Vacancy). *Adv.*  
596 *Energy Mater.* **8**, 1800409 (2018).
- 597 12. Assat, G. & Tarascon, J. M. Fundamental understanding and practical challenges of anionic redox activity in Li-ion batteries. *Nat. Energy*  
598 **3**, 373–386 (2018).
- 599 13. Assat, G., Delacourt, C., Corte, D. A. D. & Tarascon, J.-M. Editors' Choice—Practical Assessment of Anionic Redox in Li-Rich Layered  
600 Oxide Cathodes: A Mixed Blessing for High Energy Li-Ion Batteries. *J. Electrochem. Soc.* **163**, A2965–A2976 (2016).
- 601 14. Assat, G. *et al.* Fundamental interplay between anionic/cationic redox governing the kinetics and thermodynamics of lithium-rich  
602 cathodes. *Nat. Commun.* **8**, (2017).
- 603 15. Sathiya, M. *et al.* Reversible anionic redox chemistry in high-capacity layered-oxide electrodes. *Nat. Mater.* **12**, 827–835 (2013).
- 604 16. Pearce, P. E. *et al.* Evidence for anionic redox activity in a tridimensional-ordered Li-rich positive electrode β-Li2IrO3. *Nat. Mater.* **16**,  
605 580–586 (2017).
- 606 17. Perez, A. J. *et al.* Approaching the limits of cationic and anionic electrochemical activity with the Li-rich layered rocksalt Li3IrO4. *Nat.*  
607 *Energy* **2**, 954–962 (2017).
- 608 18. House, R. A. *et al.* Lithium manganese oxyfluoride as a new cathode material exhibiting oxygen redox. *Energy Environ. Sci.* **11**, 926  
609 (2018).
- 610 19. Lee, J. *et al.* Reversible Mn2+/Mn4+ double redox in lithium-excess cathode materials. *Nature* **556**, 185–190 (2018).
- 611 20. Whittingham, M. S. Electrical Energy Storage and Intercalation Chemistry. *Science (80-. ).* **192**, 1126–1127 (1976).
- 612 21. Whittingham, M. S. Lithium batteries and cathode materials. *Chem. Rev.* **104**, 4271–4301 (2004).
- 613 22. Rouxel, J. Anion-cation redox competition and the formation of new compounds in highly covalent systems. *Chem. - A Eur. J.* **2**, 1053–  
614 1059 (1996).
- 615 23. Rouxel, J. Some solid state chemistry with holes: Anion–cation redox competition in solids. *Curr. Sci.* **73**, 31–39 (1997).
- 616 24. Brec, R., Prouzet, E. & Ouvrard, G. Redox processes in the Li<sub>x</sub>FeS<sub>2</sub>/Li electrochemical system studied through crystal, Mössbauer, and  
617 EXAFS analyses. *J. Power Sources* **26**, 325–332 (1989).
- 618 25. Blandeaute, L., Ouvrard, G., Calagete, Y., Brect, R. & Rouxel, J. *Transition-metal dichalcogenides from disintercalation processes. Crystal*



619 structure determination and Mossbauer study of  $\text{Li}_x\text{FeS}$ , and its disintercalates  $\text{Li}_x\text{FeS}$ , ( $0.2 \times d \times d$ ). *J. Phys. C: Solid State Phys* **20**,  
620 (1987).

621 26. Onuk, Y., Yamanaka, S. & Kamimura, H. *ELECTROCHEMICAL CHARACTERISTICS OF TRANSITION-METAL*  
622 *TRICHALCOGENIDES IN THE SECONDARY LITHIUM BATTERY*. *Solid State Ionics* **11**, (1983).

623 27. Murphy, D. W. & Trijmbore, F. A. *METAL CHALCOGENIDES AS REVERSIBLE ELECTRODES IN NONAQUEOUS LITHIUM*  
624 *BATTERIES*. *Journal of Crystal Growth* **39**, (1977).

625 28. Murphy, D. W. The Chemistry of  $\text{TiS}_3$  and  $\text{NbSe}_3$  Cathodes. *J. Electrochem. Soc.* **123**, 960 (1976).

626 29. Whittingham, M. S. *Chemistry of intercalation compounds: Metal guests in chalcogenide hosts*. *Progress in Solid State Chemistry* **12**,  
627 (1978).

628 30. Holleck, G. L. & Driscoll, J. R. Transition metal sulfides as cathodes for secondary lithium batteries—II. titanium sulfides. *Electrochim.*  
629 *Acta* **22**, 647–655 (1977).

630 31. Whittingham, M. S. The Role of Ternary Phases in Cathode Reactions. *J. Electrochem. Soc.* **123**, 315 (1976).

631 32. Lindic, M. H. *et al.* XPS investigations of  $\text{TiO}_y\text{S}_z$  amorphous thin films used as positive electrode in lithium microbatteries. *Solid State*  
632 *Ionics* **176**, 1529–1537 (2005).

633 33. Jacobson, A. J., Chianelli, R. R., Rich, S. M. & Whittingham, M. S. *AMORPHOUS MOLYBDENUM TRISULFIDE: A NEW LITHIUM*  
634 *BATTERY CATHODE*. *Mat. Res. Bull* **14**, (1979).

635 34. Doan-Nguyen, V. V. T. *et al.* Molybdenum Polysulfide Chalcogels as High-Capacity, Anion-Redox-Driven Electrode Materials for Li-  
636 Ion Batteries. *Chem. Mater* **28**, 42 (2016).

637 35. Sakuda, A. *et al.* Amorphous Metal Polysulfides: Electrode Materials with Unique Insertion/Extraction Reactions. *J. Am. Chem. Soc.* **139**,  
638 8796–8799 (2017).

639 36. Britto, S. *et al.* Multiple Redox Modes in the Reversible Lithiation of High-Capacity, Peierls-Distorted Vanadium Sulfide. *J. Am. Chem.*  
640 *Soc* **137**, (2015).

641 37. Butala, M. M. *et al.* Local Structure Evolution and Modes of Charge Storage in Secondary Li–FeS<sub>2</sub> Cells. *Chem. Mater* **29**, (2017).

642 38. Goodenough, J. B. & Kim, Y. Locating redox couples in the layered sulfides with application to  $\text{Cu}[\text{Cr}_2]\text{S}_4$ . *J. Solid State Chem.* **182**,  
643 2904–2911 (2009).

644 39. Clark, S. J., Wang, D., Armstrong, A. R. & Bruce, P. G.  $\text{Li}(\text{V}_{0.5}\text{Ti}_{0.5})\text{S}_2$  as a 1 V lithium intercalation electrode. *Nat. Commun.* **7**, 10898  
645 (2016).

646 40. Tarascon, J. M., Disalvo, F. J., Eibschutz, M., Murphy, D. W. & Waszczak, J. V. Preparation and chemical and physical properties of the  
647 new layered phases  $\text{Li}_x\text{Ti}_{1-y}\text{MyS}_2$  with  $\text{M}=\text{V}, \text{Cr}, \text{or Fe}$ . *Phys. Rev. B* **28**, 6397–6406 (1983).

648 41. Xie, Y., Saubané, M. & Doublet, M. L. Requirements for reversible extra-capacity in Li-rich layered oxides for Li-ion batteries. *Energy*  
649 *Environ. Sci.* **10**, 266–274 (2017).

650 42. Li, B. *et al.* Thermodynamic Activation of Charge Transfer in Anionic Redox Process for Li-Ion Batteries. *Adv. Funct. Mater.* **28**, 1704864  
651 (2018).

652 43. Lu, Z. & Dahn, J. R. Understanding the Anomalous Capacity of  $\text{Li}[\text{Ni}_x\text{Li}_{(1/3-2x/3)}\text{Mn}_{(2/3-x/3)}]\text{O}_2$  Cells Using In Situ X-Ray Diffraction  
653 and Electrochemical Studies. *J. Electrochem. Soc.* **149**, A815 (2002).

654 44. Lu, Z., Beaulieu, L. Y., Donaberger, R. A., Thomas, C. L. & Dahn, J. R. Synthesis, Structure, and Electrochemical Behavior of  
655  $\text{Li}[\text{Ni}_x\text{Li}_{(1/3-2x/3)}\text{Mn}_{(2/3-x/3)}]\text{O}_2$ . *J. Electrochem. Soc.* **149**, A778–A791 (2002).

656 45. Lu, Z., MacNeil, D. D. & Dahn, J. R. Layered Cathode Materials  $\text{Li}[\text{Ni}_x\text{Li}_{(1/3-2x/3)}\text{Mn}_{(2/3-x/3)}]\text{O}_2$  for Lithium-Ion Batteries. *Electrochem.*  
657 *Solid-State Lett.* **4**, A191 (2001).

658 46. Flamary-Mespoluie, F. Synthèse et caractérisation de sulfures de métaux de transition comme matériaux d'électrode positive à forte  
659 capacité pour microbatteries au lithium, Université de Bordeaux. (2016).

660 47. Shadike, Z. *et al.* Antisite occupation induced single anionic redox chemistry and structural stabilization of layered sodium chromium  
661 sulfide. *Nat. Commun.* **8**, 566 (2017).

662 48. Sakuda, A. *et al.* A Reversible Rocksalt to Amorphous Phase Transition Involving Anion Redox. *Sci. Rep.* **8**, 15086 (2018).

- 663 49. Sakuda, A. *et al.* Rock-salt-type lithium metal sulphides as novel positive-electrode materials. *Sci. Rep.* **4**, 2–6 (2014).
- 664 50. Matsunaga, T. *et al.* Dependence of Structural Defects in Li<sub>2</sub>MnO<sub>3</sub> on Synthesis Temperature. *Chem. Mater.* **28**, 4143–4150 (2016).
- 665 51. Furuseth, S., Brattås, L., Kjekshus, A., Andresen, A. F. & Fischer, P. On the Crystal Structures of TiS<sub>3</sub>, ZrS<sub>3</sub>, ZrSe<sub>3</sub>, ZrTe<sub>3</sub>, HfS<sub>3</sub>, and HfSe<sub>3</sub>. *Acta Chem. Scand.* **29a**, 623–631 (1975).
- 667 52. Chamas, M., Sougrati, M.-T., Reibel, C. & Lippens, P.-E. Quantitative Analysis of the Initial Restructuring Step of Nanostructured FeSn<sub>2</sub>-Based Anodes for Li-Ion Batteries. *Chem. Mater.* **25**, 2410–2420 (2013).
- 668 53. Fatseas, G. A. & Goodenough, J. B. Mössbauer <sup>57</sup>Fe spectra exhibiting “ferrous character”. *J. Solid State Chem.* **33**, 219–232 (1980).
- 669 54. Vaughan, D. J. & Ridout, M. S. Mössbauer studies of some sulphide minerals. *J. Inorg. Nucl. Chem.* **33**, 741–746 (1971).
- 671 55. Michael Bancroft, G., Kasrai, M., Fleet, M. & Stn, C. S K- AND L-EDGE X-RAY ABSORPTION SPECTROSCOPY OF METAL SULFIDES AND SULFATES: APPLICATIONS IN MINERALOGY AND GEOCHEMISTRY. *Can. Mineral.* **33**, 949–960 (1995).
- 672 56. Fleet, M. E. XANES SPECTROSCOPY OF SULFUR IN EARTH MATERIALS. *Can. Mineral.* **43**, 1811–1838 (2005).
- 673 57. Kowalska, J. K. *et al.* Iron L<sub>2,3</sub>-Edge X-ray Absorption and X-ray Magnetic Circular Dichroism Studies of Molecular Iron Complexes with Relevance to the FeMoco and FeVco Active Sites of Nitrogenase. *Inorg. Chem.* **56**, 8147–8158 (2017).
- 674 58. Zhang, L. *et al.* Tracking the Chemical and Structural Evolution of the TiS<sub>2</sub> Electrode in the Lithium-Ion Cell Using Operando X-ray Absorption Spectroscopy. *Nano Lett* **18**, 4506–4515 (2018).
- 675 59. Farrell, S. P. *et al.* Evolution of local electronic structure in alabandite and niningerite solid solutions [(Mn,Fe)S, (Mg,Mn)S, (Mg,Fe)S] using sulfur K - and L -edge XANES spectroscopy. *Am. Mineral.* **87**, 1321–1332 (2002).
- 676 60. Yang, W. & Devereaux, T. P. Anionic and cationic redox and interfaces in batteries: Advances from soft X-ray absorption spectroscopy to resonant inelastic scattering. *J. Power Sources* **389**, 188–197 (2018).
- 677 61. Szilagy, R. K. *et al.* Description of the Ground State Wave Functions of Ni Dithiolenes Using Sulfur K-edge X-ray Absorption Spectroscopy. *J. Am. Chem. Soc.* **125**, 9158–9169 (2003).
- 678 62. Fleet, M. E., Harmer, S. L., Liu, X. & Nesbitt, H. W. Polarized X-ray absorption spectroscopy and XPS of TiS<sub>3</sub>: S K- and Ti L-edge XANES and S and Ti 2p XPS. *Surf. Sci.* **584**, 133–145 (2005).
- 679 63. Matsuyama, T. *et al.* Structure analyses using X-ray photoelectron spectroscopy and X-ray absorption near edge structure for amorphous MS<sub>3</sub>(M: Ti, Mo) electrodes in all-solid-state lithium batteries. *J. Power Sources* **313**, 104–111 (2016).
- 680 64. Martinez, H. *et al.* Influence of the cation nature of high sulfur content oxysulfide thin films MO<sub>y</sub>S<sub>z</sub> (M<sup>1/4</sup>W, Ti) studied by XPS. *Appl. Surf. Sci.* **236**, 377–386 (2004).
- 681 65. Strehle, B. *et al.* The Role of Oxygen Release from Li- and Mn-Rich Layered Oxides during the First Cycles Investigated by On-Line Electrochemical Mass Spectrometry. *J. Electrochem. Soc.* **164**, A400–A406 (2017).
- 682 66. Boulton, A. & Louer, D. Indexing of powder diffraction patterns for low-symmetry lattices by the successive dichotomy method. *J. Appl. Cryst.* **24**, 987–993 (1991).
- 683 67. Rodríguez-Carvajal, J. *FullProf Suite; all the programs can be obtained from: <http://www.ill.eu/sites/fullprof>.*
- 684 68. Fehse, M. *et al.* The Electrochemical Sodiation of FeSb<sub>2</sub>: New Insights from Operando <sup>57</sup>Fe Synchrotron Mössbauer and X-Ray Absorption Spectroscopy. *Batter. Supercaps* **2**, 66–73 (2019).
- 685 69. Qiao, R. *et al.* High-efficiency in situ resonant inelastic x-ray scattering (iRIXS) endstation at the Advanced Light Source. *Rev. Sci. Instrum.* **88**, (2017).
- 686 70. Shirley, D. A. High-resolution X-Ray photoemission spectrum of the valence bands of gold. *Phys. Rev. B* **5**, 4709–4714 (1972).
- 687 71. Scofield, J. H. Hartree-Slater subshell photoionization cross-sections at 1254 and 1487 eV. *J. Electron Spectros. Relat. Phenomena* **8**, 129–137 (1976).
- 688 72. Ping Ong, S. *et al.* Python Materials Genomics (pymatgen): A robust, open-source python library for materials analysis. *Comput. Mater. Sci.* **68**, 314–319 (2013).
- 689 73. Kresse, G. & Joubert, D. From ultrasoft pseudopotentials to the projector augmented-wave method. *Phys. Rev. B* **59**, 1758–1775 (1999).
- 690 74. Perdew, J. P., Burke, K. & Ernzerhof, M. Generalized Gradient Approximation Made Simple. *Phys. Rev. Lett.* **77**, 3865–3868 (1996).
- 691
- 692
- 693
- 694
- 695
- 696
- 697
- 698
- 699
- 700
- 701
- 702
- 703
- 704
- 705

- 706 75. Grimme, S., Ehrlich, S. & Goerigk, L. Effect of the damping function in dispersion corrected density functional theory. *J. Comput. Chem.*  
707 **32**, 1456–1465 (2011).
- 708 76. Dudarev, S. L., Botton, G. A., Savrasov, S. Y., Humphreys, C. J. & Sutton, A. P. Electron-energy-loss spectra and the structural stability  
709 of nickel oxide: An LSDA+U study. *Phys. Rev. B* **57**, 1505–1509 (1998).
- 710